JEM Journal of Experimental Medicine

ARTICLE

Tumor-derived OBP2A promotes prostate cancer castration resistance

Ji-Hak Jeong[1,2*], Shangwei Zhong[1,3*], Fuzhuo Li[4], Changhao Huang[1], Xueyan Chen[1], Qingqing Liu[3], Shoujiao Peng[1], HaJeung Park[5], You Mie Lee[2], Jasreman Dhillon[6], and Jun-Li Luo[1,3]

Androgen deprivation therapy (ADT) is a systemic therapy for advanced prostate cancer (PCa); although most patients initially respond to ADT, almost all cancers eventually develop castration-resistant PCa (CRPC). Currently, most research focuses on castration-resistant tumors, and the role of tumors in remission is almost completely ignored. Here, we report that odorant-binding protein (OBP2A) released from tumors in remission during ADT catches survival factors, such as CXCL15/IL8, to promote PCa cell androgen-independent growth and enhance the infiltration of myeloid-derived suppressor cells (MDSCs) into tumor microenvironment, leading to the emergence of castration resistance. OBP2A knockdown significantly inhibits CRPC and metastatic CRPC development and improves therapeutic efficacy of CTLA-4/PD-1 antibodies. Treatment with OBP2A-binding ligand α-pinene interrupts the function of OBP2A and suppresses CRPC development. Furthermore, α-pinene–conjugated doxorubicin/docetaxel can be specifically delivered to tumors, resulting in improved anticancer efficacy. Thus, our studies establish a novel concept for the emergence of PCa castration resistance and provide new therapeutic strategies for advanced PCa.

Introduction

Prostate cancer (PCa) is the most common malignancy and the second-leading cause of cancer-related mortality in men in Western countries (Amaral et al., 2012; Karantanos et al., 2013; Pernar et al., 2018). Androgen deprivation therapy (ADT) was first used in 1941 and still remains the principal and backbone treatment for patients with advanced PCa, as the majority of patients respond to ADT with a mean remission time of 2 to 3 yr. However, almost all cancers eventually develop castration resistance (Crawford et al., 2019; Karantanos et al., 2013). Understanding the mechanisms that underlie the pathogenesis of castration resistance is of paramount importance for the development of novel therapeutic approaches for this disease.

It has been suggested that the progression of PCa to castration resistance under ADT is a complex process that involves outgrowth of preexisting clones of androgen-independent (AI) cancer stem cells (Amaral et al., 2012; Karantanos et al., 2013), adaptive activation or suppression of signaling pathways that help the cancer cells survive and grow, as well as the remodeling of tumor microenvironment (TME) under androgen depletion (Ammirante et al., 2010; Jeong et al., 2017; So et al., 2005). However, current research has mostly focused on the tumors that have already been castration-resistant (Alibhai et al., 2006; Amaral et al., 2012; Ammirante et al., 2010; Jeong et al., 2017; Karantanos et al., 2013; Montironi et al., 2006); almost no attention has been paid to the role of the substances released from tumors at the remission stage during ADT in the emergence of PCa castration resistance.

The odorant-binding protein 2A (OBP2A) is a small extracellular protein belonging to the lipocalin superfamily, which is thought to transport small, hydrophobic, volatile molecules, or odorants through the nasal mucus to olfactory receptors and may also function as a scavenger of highly concentrated or toxic odors (Tcatchoff et al., 2006). OBP2A has a hydrophobic cavity within its beta-barrel, which facilitates the reversible binding of small molecular odorants and the delivering of the odorants to the olfactory receptors (Briand et al., 2002; Lacazette et al., 2000; Pelosi, 2001). OBP2A regulates glucose and lipid metabolism and has been linked to hepatic steatosis and type 2 diabetes (Cho et al., 2011; Sheng et al., 2011; Zhou and Rui, 2013). The role of OBP2A in cancer is unclear. The α-pinene, the main

[1]Department of Molecular Medicine, The Scripps Research Institute, Jupiter, FL, USA; [2]Vessel-Organ Interaction Research Center (VOICE, MRC), College of Pharmacy, Kyungpook National University, Daegu, South Korea; [3]The Cancer Research Institute, Hengyang Medical School, University of South China, Hengyang, China; [4]Department of Chemistry, The Scripps Research Institute, Jupiter, FL, USA; [5]X-ray Core Facility, The Scripps Research Institute, Jupiter, FL, USA; [6]Department of Pathology, Moffitt Cancer Center, Tampa, FL, USA.

*J.-H. Jeong and S. Zhong contributed equally to this paper. Correspondence to Jun-Li Luo: jlluo@usc.edu.cn.

component of coniferous tree oils, is a naturally occurring OBP2A-binding ligand (Briand et al., 2002; Whitson and Whitson, 2014), which has been used as an effective bronchodilator for the treatment of asthma (Salehi et al., 2019). It has also been reported that α-pinene has antioxidant, antimicrobial, and anticancer activities (Aydin et al., 2013; Zhao et al., 2018).

TME constituted of cellular and noncellular components is a complicated and dynamic system and is an indispensable part of tumor as a whole (Gabrilovich, 2017; Gabrilovich et al., 2012; Zhong et al., 2020). One of the major cell components in the TME is myeloid-derived suppressor cells (MDSCs), which are a heterogeneous population of myeloid lineage with an immature phenotype that expand in response to various tumor-derived cytokines and chemokines (Gabrilovich, 2017; Gabrilovich et al., 2012; Zhong et al., 2020). MDSCs in TME play important roles in tumor growth, progression, and metastasis through releasing various growth factors and affecting the interactions between cancer cells and immune effectors (Gabrilovich, 2017; Gabrilovich et al., 2012).

Here, we show that OBP2A is highly expressed in tumors in remission during ADT. OBP2A secreted from cancer cells of tumors in remission catches the survival factors, such as CXCL15/IL8, to promote PCa cell androgen-independent growth and to attract the infiltration of MDSCs into TME, leading to the emergence of castration resistance. OBP2A knockdown significantly inhibits CRPC and metastatic CRPC (mCRPC) development, and improves the efficacy of CTLA-4 and PD-1 antibodies for the suppression of CRPC. Treatment with α-pinene interrupts the interaction of OBP2A with CXCL15/IL8 and suppresses CRPC development. Engineered α-pinene–conjugated doxorubicin (DOX) and docetaxel (DTX) are specifically delivered to and accumulated in tumors, resulting in a much stronger anticancer efficacy.

Results

OBP2A is highly expressed in and secreted from PCa cells of tumors in remission during ADT

To investigate the mechanisms underlying the emergence of PCa castration resistance, we employed a PCa allograft mouse model that mimics human CRPC development (Ammirante et al., 2010; Jeong et al., 2017; Watson et al., 2005). In this model, an androgen receptor (AR)–positive and androgen-dependent mouse PCa cell line, Myc-CaP, which was isolated from a *c-Myc* transgenic PCa mouse with PCa (Watson et al., 2005), was employed. Myc-CaP cells can grow as tumors in immune competent FVB male mice in an androgen-dependent manner, when host mice are castrated, and Myc-CaP allografts shrink and later regrow and become AR-positive CRPC (Ammirante et al., 2010; Jeong et al., 2017; Watson et al., 2005; Fig. 1 A).

Using RNA sequencing (RNA-seq) analysis (Gene Expression Omnibus accession no. GSE208321), we compared the gene expression spectrum among primary PCa (PPC), shrunk PCa (S-PC), and castration-resistant PCa (CRPC) tissues, and among purified cancer cells isolated from PPC, S-PC, and CRPC tissues (Fig. 1 A). We analyzed the RNA-seq data and presented lists of top 25 down-regulated genes and top 78 up-regulated genes in S-PC cells as compared with PPC and CRPC cells using a heatmap (Fig. S1 A). We analyzed the KEGG pathway that up- or down-regulated in S-PC or CRPC as compared with PPC. We found that "cytokine–cytokine receptor interaction" was the most down-regulated in CRPC, while "systemic lupus erythematosus" was the most up-regulated in CRPC (Fig. S1 B). "Metabolic pathway" was the most down-regulated in S-PC, while "pathways in cancer" was the most up-regulated in S-PC (Fig. S1 C).

Based on RNA-seq data, the expression of a group of genes was very significantly increased in S-PC tumors, in which OBP2A was one of the most increased gene in S-PC cells. The expressions of OBP2A mRNA and protein are highly increased in S-PC tumor tissues (Fig. 1, B and C; and Fig. S1 D) and in purified tumor cells (Fig. 1, D and E). Similarly, the expression of OBP2A was significantly increased in S-PC tumors collected from human PCa LNCaP xenograft mouse models (Fig. S1 E). To further confirm whether the expression of OBP2A is highly expressed in human S-PC tumors, we analyzed the expression of OBP2A in human PCa patient-derived xenograft (PDX) models. We found that the expressions of OBP2A were significantly increased in S-PC tumors in PCa PDX models (Fig. 1 F). Furthermore, we found that the expression of OBP2A protein in prostate tumors started to increase 4 d after castration and was undetectable by Western blot 24 d after castration in Myc-CaP allograft mouse models (Fig. 1 G). In addition, we compared the expression levels of OBP2A mRNA in Myc-CaP cells cultured in normal medium versus charcoal-treated medium at different time points, we found that the expression level of OBP2A in Myc-CaP cells cultured in charcoal-treated medium was gradually increased, started at day 2 and peaked at day 8 (Fig. 1 H). Similarly, the expression of OBP2A mRNA in androgen-sensitive human PCa LNCaP and VCaP cells was also gradually increased when cultured in charcoal-treated medium (Fig. S1, F and G).

OBP2A promotes CRPC development

To test the role of OBP2A in PCa development, we established stable OBP2A knockdown (OBP2A-KD) cell lines by infecting Myc-CaP and LNCaP cells with mouse or human OBP2A shRNA lentivirus and selected by puromycin treatment (Fig. 2 A and Fig. S2 A). We compared the proliferation rate between OBP2A knockdown and control cells by 3-(4,5-dimethylthiazol-2-yl)-2,5 diphenyl tetrazolium bromide (MTT) assay, we found that OBP2A knockdown did not affect Myc-CaP and LNCaP cell proliferation cultured in normal or charcoal-treated medium (Fig. 2 B and Fig. S2 B, and C). OBP2A knockdown had no effect on primary Myc-CaP allograft tumor development, while significantly inhibited Myc-CaP CRPC development in FVB male mice (Fig. 2 C and Fig. S2 D). Similarly, OBP2A knockdown significantly inhibited LNCaP xenograft CRPC development in *Rag1*$^{-/-}$ male mice (Fig. 2 D and Fig. S2 E).

Based on the expression pattern of OBP2A in PCa during ADT (Fig. 1 G), we manipulated the expression level of OBP2A in Myc-CaP cells by infecting Myc-CaP cells with adenovirus that was engineered to express HA-OBP2A (Fig. S2 F). The infected cells kept the expression of HA-OBP2A for about 10 d. We found that exogenous expression of OBP2A did not affect the proliferation rate of Myc-CaP cells cultured in normal or charcoal-treated

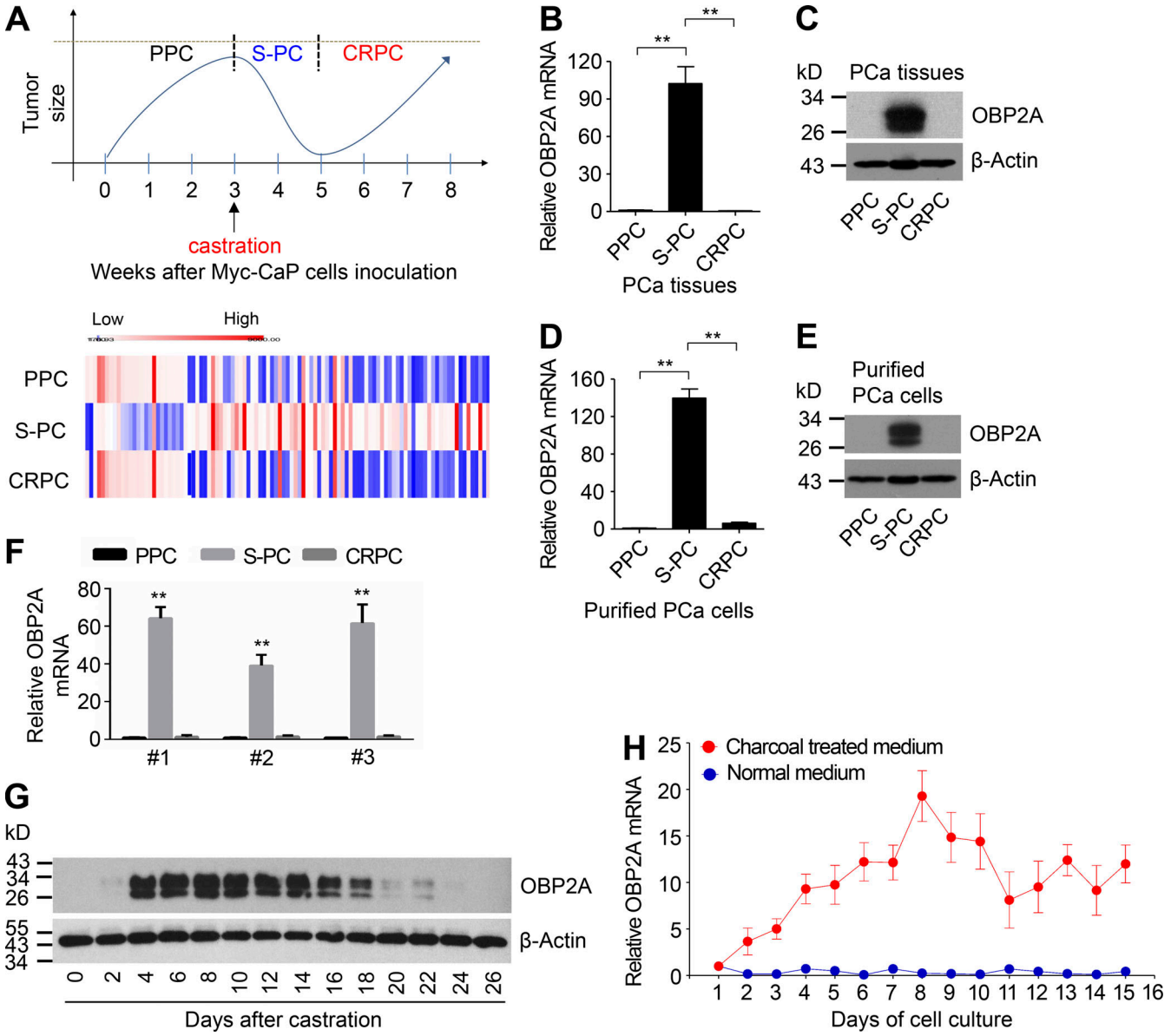

Figure 1. **The expression of OBP2A is highly increased in shrunk tumors during ADT. (A)** The diagram of different time points for allograft tumor collection and tumor cell purification in Myc-CaP castrate-resistant PCa mouse model (upper panel), and the RNA-seq or microarray analysis (lower panel) of PPC, S-PC, and CRPC. **(B)** Real-time PCR analysis for OBP2A mRNA expression in PPC, S-PC, and CRPC tissues. Error bars represent mean ± SD; *n* = 3/group and analyzed by Student's *t* test. **, P < 0.01. **(C)** Western blot analysis for OBP2A protein expression in PPC, S-PC, and CRPC tissues. **(D)** Real-time PCR analysis for OBP2A mRNA expression in purified cancer cells of PPC, S-PC, and CRPC. Error bars represent mean ± SD; *n* = 3/group and analyzed by Student's *t* test. **, P < 0.01. **(E)** Western blot analysis for OBP2A protein expression in purified cancer cells of PPC, S-PC, and CRPC. **(F)** The expression of OBP2A is significantly increased in S-PC tumors of human PCa PDX model. qRT-PCR analysis for the expression of OBP2A in PPC, S-PC, and CRPC of human PCa PDX model. Three cohorts of tumors from three different human PCa PDX models derived from three cases of human PCa tissues. Error bars represent mean ± SD; *n* = 3/group and analyzed by Student's *t* test. **, P < 0.01. **(G)** Western blot analysis for OBP2A protein expression in PCa tissues collected from Myc-CaP allograft mouse model at different time points after castration. **(H)** Real-time PCR analysis for OBP2A mRNA expression in Myc-CaP cells collected at different time points after cultured in charcoal-treated medium. Error bars represent mean ± SD; *n* = 3/group. Each panel in B–H is representative of at least two independent experiments. See also Fig. S1. Source data are available for this figure: SourceData F1.

medium (Fig. 2, E and F). Furthermore, 5 × 10^4 Myc-CaP cells infected with control or OBP2A expression (OBP2A-OE) adenovirus were mixed with matrigel and inoculated s.c. into the flank of 6-wk-old castrated FVB male mice. Consistently, we found that OBP2A overexpression significantly promoted CRPC development (Fig. 2 G and Fig. S2 G). Together, these results indicate that OBP2A plays an important role in CRPC development.

OBP2A promotes mCRPC development

To investigate the role of OBP2A in mCRPC development, an orthotopic metastatic PCa model in immune competent FVB male mice was employed. Tumor tissues, derived from OBP2A-KD or control Myc-CaP cells, were harvested from s.c. allograft tumors in FVB male mice and cut into pieces of about 1 mm^3. A tumor tissue (1 mm^3) was grafted into the anterior prostates of

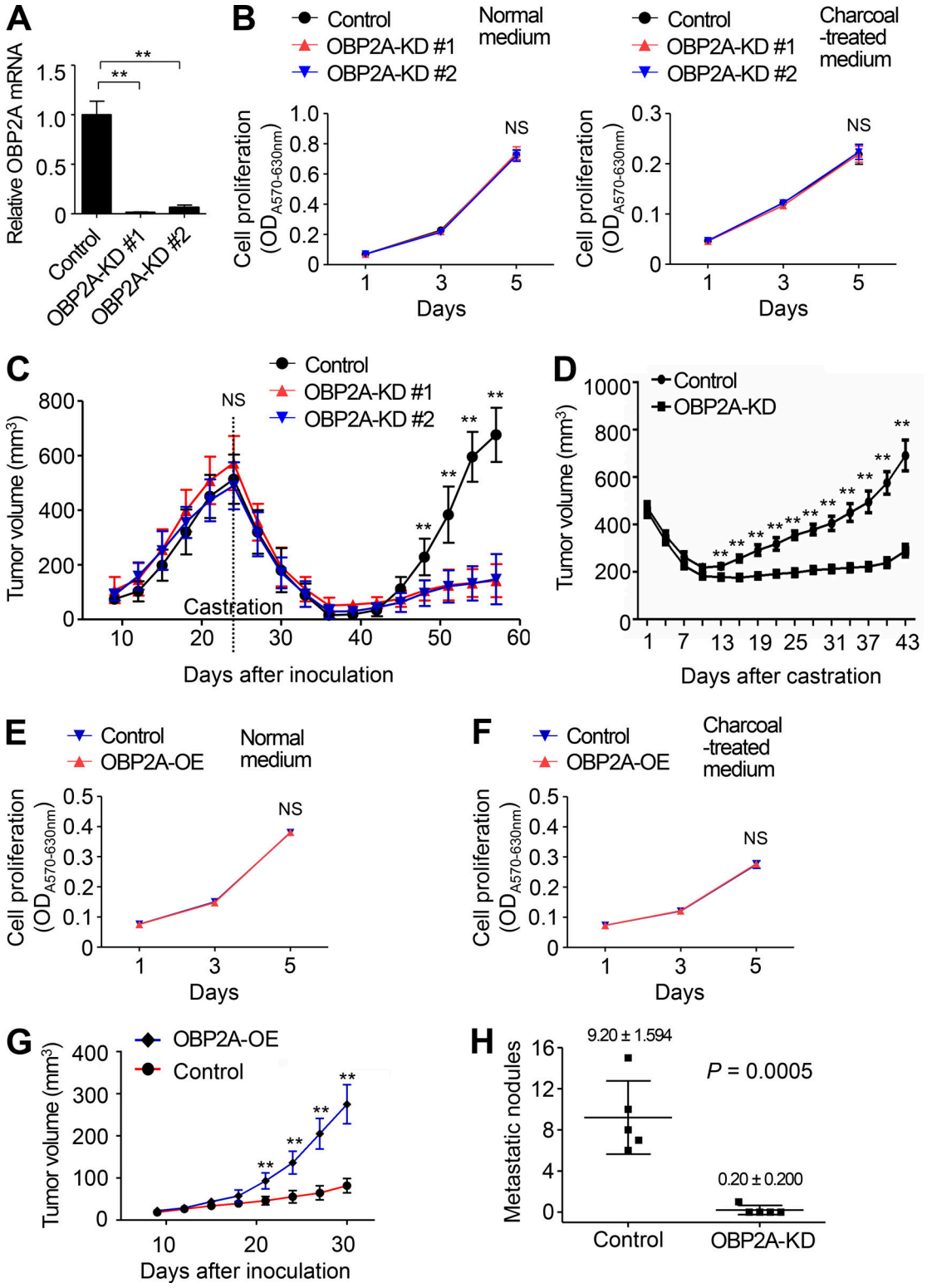

Figure 2. **OBP2A promotes CRPC and mCRPC development. (A)** Real-time PCR analysis for OBP2A mRNA expression in control and OBP2A stable knockdown (OBP2A-KD) Myc-CaP cells cultured in charcoal-treated medium. Error bars represent mean ± SD; *n* = 3/group and analyzed by Student's *t* test. **, P < 0.01. **(B)** MTT assay for the proliferation rate of control or OBP2A-KD Myc-CaP cells cultured in normal (left) or charcoal-treated (right) medium. Error bars represent mean ± SD; *n* = 3/group and analyzed by Student's *t* test. **(C)** Allograft tumor development in FVB male mice inoculated with 1 × 10^6 control or OBP2A-KD Myc-CaP cells. Error bars represent mean ± SD; *n* = 5/group and analyzed by Student's *t* test. **, P < 0.01. **(D)** Xenograft tumor development in *Rag1*$^{-/-}$ male mice inoculated with 1 × 10^7 control or OBP2A-KD LNCaP cells. Error bars represent mean ± SD; *n* = 5/group and analyzed by Student's *t* test. **, P < 0.01. **(E and F)** MTT assay for the proliferation rate of Myc-CaP cells infected with control or OBP2A overexpression (OBP2A-OE) adenovirus in normal (E) or charcoal-treated (F) medium. Error bars represent mean ± SD; *n* = 3/group and analyzed by Student's *t* test. **(G)** Allograft tumor development in castrated

FVB male mice inoculated with Myc-CaP cells infected with 5 × 10^4 control or OBP2A overexpression (OBP2A-OE) adenovirus. Error bars represent mean ± SD; n = 5/group and analyzed by Student's t test. **, P < 0.01. **(H)** The comparison of the incidences of lymph node metastasis between control and OBP2A-KD Myc-CaP tumors in an orthotopic metastatic PCa mouse model. Error bars represent mean ± SD; n = 5/group and analyzed by Student's t test. Each panel in A–H is representative of at least two independent experiments. See also Fig. S2.

6-wk-old FVB male mice, and at the time of transplantation mice were castrated. 6 wk after grafting, mice were sacrificed. We found that control mice had many metastases in lymph nodes, and OBP2A knockdown significantly reduced PCa metastasis (Fig. 2 H and Fig. S2 H), suggesting that OBP2A promotes mCRPC development.

OBP2A interacts with CXCL15/IL8 to promote PCa cell proliferation and migration

OBP2A knockdown did not affect the proliferation of Myc-CaP and LNCaP cells cultured in charcoal-treated medium in which androgen and many other growth factors were stripped or reduced, while OBP2A knockdown significantly inhibited CRPC development in mouse models (Fig. 2 and Fig. S2), suggesting that OBP2A-induced CRPC development may be related to TME. To test this hypothesis and based on the data from RNA-seq and microarray, we screened the expression of cytokines/chemokines and growth factors by real-time PCR in PPC, S-PC, and CRPC tumor tissues as well as in purified tumor cells (Fig. S3 A). We found that as compared with PPC tumors, the expression of chemokine (C-X-C motif) ligand 15 (CXCL15) was very significantly increased in S-PC tumor tissues (>200 times), and increased in CRPC tumor tissues (20–40 times; Fig. 3 A and Fig. S3 A). In contrast, the expression levels of CXCL15 mRNA in purified S-PC and CRPC tumor cells were much lower than in S-PC and CRPC tumor tissues, although they were increased in S-PC and CRPC tumor cells as compared with PPC tumor cells (Fig. 3 B and Fig. S3 B). Consistently, CXCL15 protein was highly expressed in S-PC tissues (Fig. 3 C). These results indicate that stromal cells in TME rather than cancer cells are the major source of CXCL15 in S-PC tissues. Supporting this, co-immunofluorescence staining of CXCL15 with T cells, B cells, and macrophages showed that macrophages were one of the CXCL15 sources in S-PC tissues (Fig. S3 C).

Importantly, we found that OBP2A and CXCL15 could be co-immunoprecipitated by each other in S-PC tissue lysates (Fig. 3 D). Immunofluorescence (IF) staining showed that the expression and co-localization of OBP2A and CXCL15 in S-PC tumors collected from Myc-CaP allograft mouse models (Fig. 3 E). CXCL15 is a small chemokine that belongs to the CXC chemokine family and is increased in response to some physiological and pathological conditions, such as allergic inflammation (Zhao et al., 2005). The human homolog of CXCL15 is IL8. Three-dimensional structure simulation and prediction supports the interaction between OBP2A and CXCL15/IL8 of both mouse and human origin (Fig. 3 F). Furthermore, we found that treatment with CXCL15/IL8 significantly promoted the proliferation of control cells but not OBP2A-KD Myc-CaP (Fig. 3 G) and LNCaP (Fig. S3 D) cells cultured in charcoal-treated medium. Transwell migration assay showed that OBP2A-KD Myc-CaP and LNCaP cells significantly lost the attraction in response to CXCL15/IL8 as compared with control cells (Fig. 3 H and Fig. S3, E and F). Together, these results suggest that OBP2A secreted from PCa cells under androgen depletion promotes PCa cell growth and migration through interaction with CXCL15/IL8.

OBP2A promotes the infiltration of MDSCs into S-PC tumors

MDSCs play important roles in the maintenance of the immunosuppressive TME through affecting the interactions between cancer cells and immune effectors (Gabrilovich, 2017; Gabrilovich et al., 2012). CD11b, Gr1, and CXCR2 are the markers of MDSCs (Bronte et al., 2016; Yang et al., 2020). We examined the expression of CD11b, Gr1, and CXCR2 in OBP2A-KD and control S-PC tissues, and we found that the expression of CD11b, Gr1, and CXCR2 was significantly reduced in OBP2A-KD S-PC tissues (Fig. 4 A). Consistently, IF staining of Gr1 further showed the significant reduction of MDSCs in OBP2A-KD S-PC tissues (Fig. 4 B). To confirm the suppressive effects of MDSCs on T cells, MDSCs suppression assay was performed by coculturing T cells with MDSCs isolated from S-PC tumors. We found that the suppression of MDSCs on T cell proliferation was significant and dose-dependent (Fig. 4 C). In addition, transwell migration assay showed that knockdown of OBP2A in LNCaP cells significantly decreased the capability of LNCaP cells to attract U937 cells when cultured in charcoal-treated medium (Fig. S4, A and B). These results suggest that OBP2A from PCa cells promotes the infiltration of MDSCs into S-PC tumors.

In addition, we examined whether OBP2A causes monocytes to differentiate into MDSCs. We employed in vitro co-culture system, in which SC cells established from human peripheral blood mononuclear cells were co-cultured with control or OBP2A-oe LNCaP cells in charcoal-treated medium for 7 d (Fig. S4, C and D). The expression of CD33, which is one of the key markers of human MDSC (Cassetta et al., 2019; Lechner et al., 2011), was analyzed. We found that there were no significant differences of CD33 mRNA expression in SC cells co-cultured with control or OBP2A-oe LNCaP cells (Fig. S4 E), suggesting that OBP2A does not cause monocytes to differentiate into MDSCs. To examine whether OBP2A plays a key role in the recruitment of MDSCs, SC cells were differentiated into MDSCs through IL-6 and GM-CSF treatment for 7 d (Fig. S4 F; Lechner et al., 2010), and then co-cultured with control or OBP2A-oe LNCaP cells using a transwell migration chamber containing charcoal-treated medium for 24 h (Fig. S4 G). We found that OBP2A overexpression in LNCaP cells significantly increased the migration of MDSCs (Fig. S4 H). We also found that OBP2A knockdown in LNCaP cells significantly decreased the migration of MDSCs (Fig. S4, I–K). These results suggest that OBP2A contributes to the recruitment of MDSCs but not the differentiation of peripheral blood mononuclear cells into MDSCs.

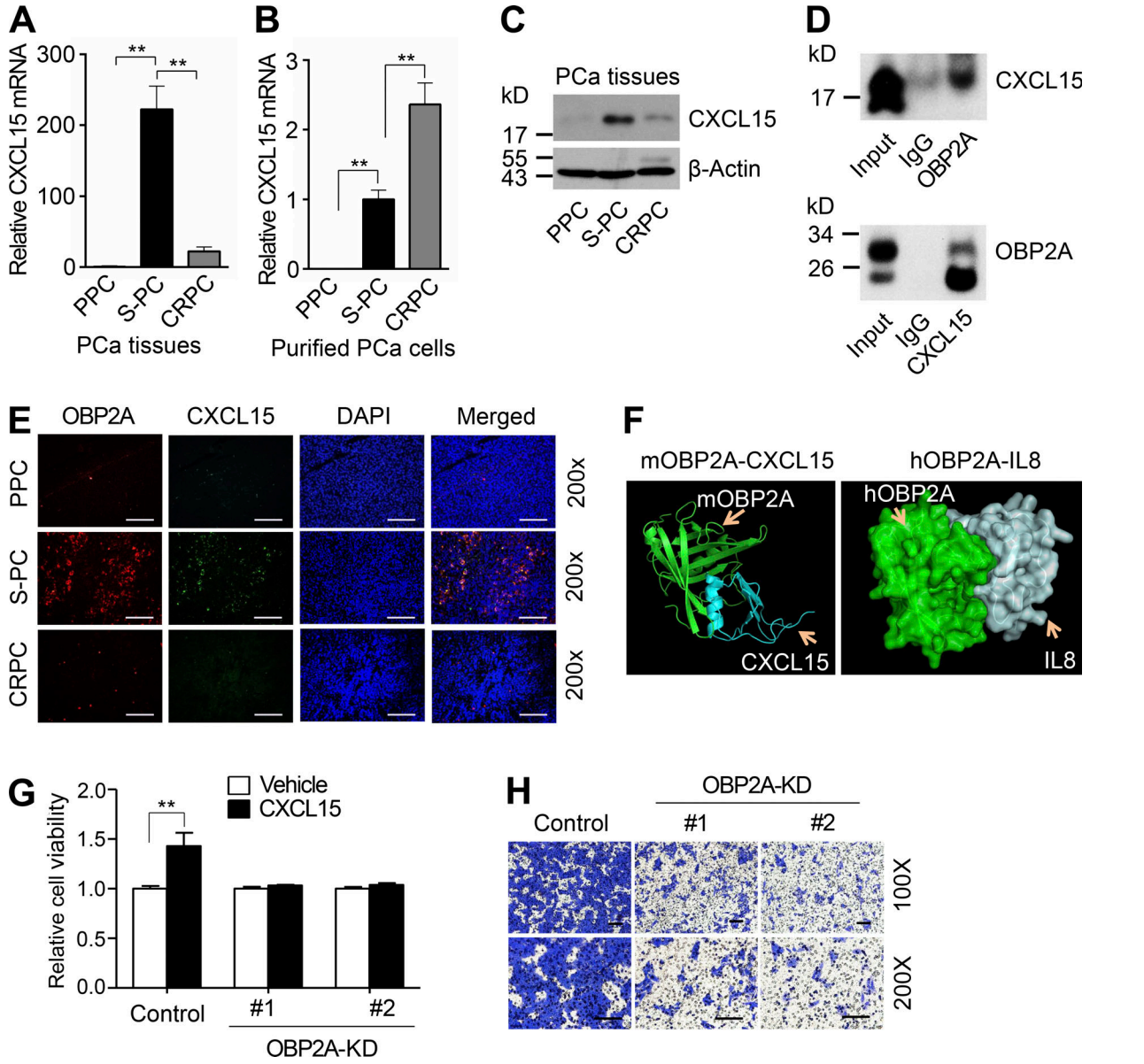

Figure 3. **OBP2A interacts with CXCL15/IL8 to promote PCa cell proliferation and migration. (A)** Real-time PCR analysis for CXCL15 mRNA expression in PPC, S-PC, and CRPC tissues collected from Myc-CaP allograft mouse models. Error bars represent mean ± SD; *n* = 3/group and analyzed by Student's *t* test. **, P < 0.01. **(B)** Real-time PCR analysis for CXCL15 mRNA expression in purified cells of PPC, S-PC, and CRPC. Error bars represent mean ± SD; *n* = 3/group and analyzed by Student's *t* test. **, P < 0.01. **(C)** Western blot analysis for CXCL15 protein expression in PPC, S-PC, and CRPC tissues collected from Myc-CaP allograft mouse models. **(D)** Immunoprecipitation assay for the interaction between OBP2A and CXCL15. Cell lysates from S-PC tumor tissues were subjected to co-immunoprecipitation (Co-IP) using OBP2A antibody, followed by Western blot using CXCL15 antibody (upper panel), or co-immunoprecipitation using CXCL15 antibody, followed by Western blot using OBP2A antibody (lower panel). **(E)** IF staining of OBP2A and CXCL15 in PPC, S-PC, and CRPC tissues. The scale bars represent 100 µm. **(F)** 3D structure simulation of the interaction between mouse OBP2A and CXCL15 (left), or human OBP2A and IL8 (right). **(G)** MTT assay for the proliferation rate of control and OBP2A-KD Myc-CaP cells treated with vehicle or CXCL15 (100 ng/ml) in charcoal-treated medium for 72 h. Error bars represent mean ± SD; *n* = 3/group and analyzed by Student's *t* test. **, P < 0.01. **(H)** Representative images of transwell migration assay for control and OBP2A-KD Myc-CaP cells cultured in 1% charcoal-treated medium, and 100 ng/mLCXCL15 or vehicle was added in the lower chamber. The scale bars represent 100 µm. Each panel in A–E, G, and H is representative of at least two independent experiments. See also Fig. S3. Source data are available for this figure: SourceData F3.

OBP2A knockdown enhances the anticancer efficacy of anti–PD-1 and CTLA-4 antibodies in mouse models

The immune checkpoint inhibitors, such as the CTLA-4 and PD-1 antibodies, have been successful in treating some types of cancers with a high tumor mutational burden, however, they have not worked well in PCa (Boettcher et al., 2019; Zhong et al., 2020). We examined the expression level of PD-1, PD-L1, CTLA-4, and CD86 in PPC, S-PC, and CRPC tissues, and found that all of them were significantly increased in S-PC tissues as compared with PPC or CRPC tumors (Fig. 4 D). Importantly, treatment with anti–PD-1 or CTLA-4 antibody had no or very mild effect on CRPC development, while knockdown of OBP2A in cancer cells very

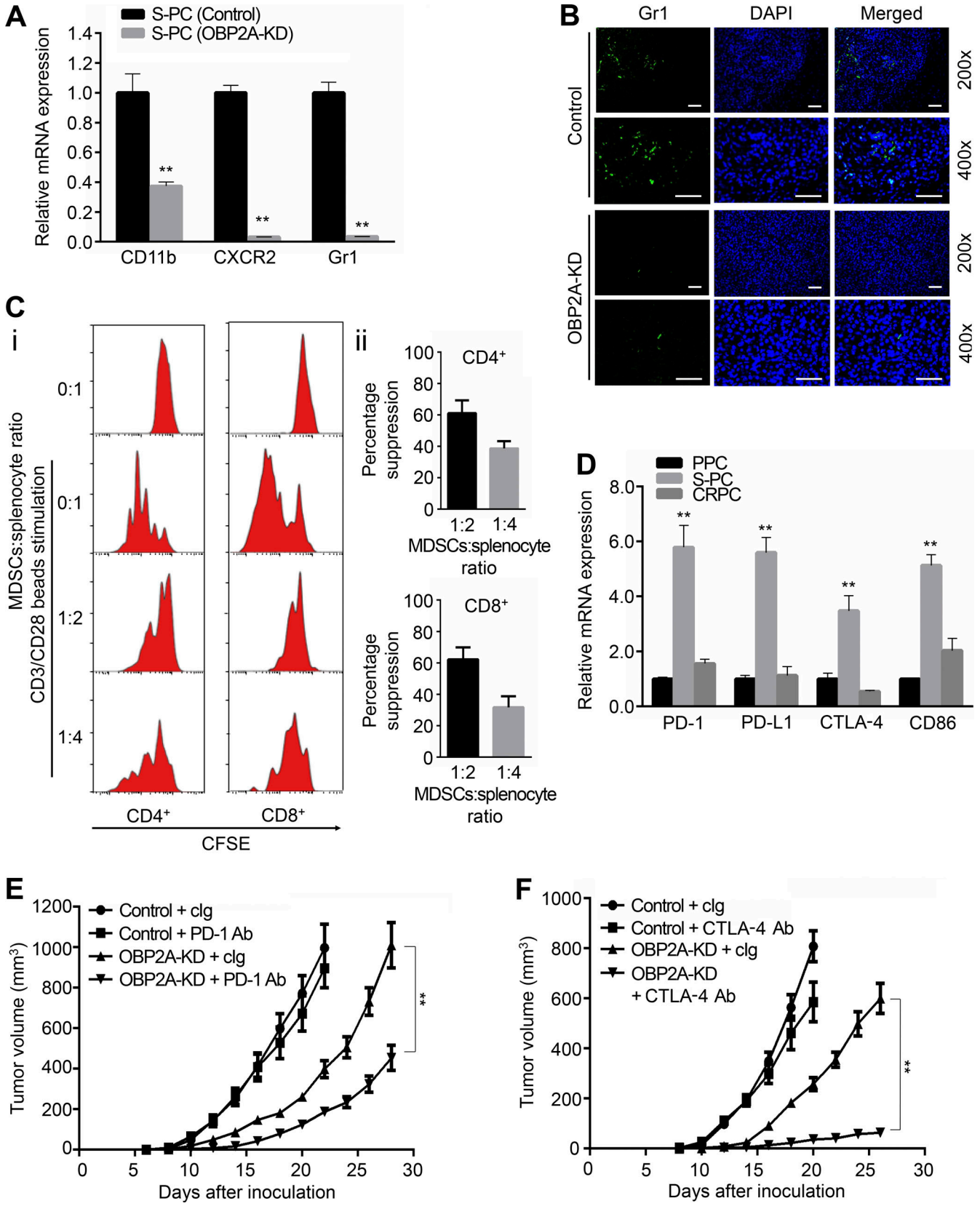

Figure 4. **OBP2A knockdown decreases the infiltration of MDSCs in TME and enhances the anti-tumor efficacy of PD-1 and CTLA-4 antibody therapy.** **(A)** Real-time PCR analysis for the expression of CD11b, CXCR2, and Gr1 mRNA expression in S-PC tissues collected from control and OBP2A-KD Myc-CaP allograft mouse models. Error bars represent mean ± SD; *n* = 3/group and analyzed by Student's *t* test. **, P < 0.01. **(B)** IF analysis for the expression of Gr1 protein in S-PC tissues collected from control and OBP2A-KD Myc-CaP allograft mouse models. The scale bars represent 50 µm. **(C)** The MDSCs suppression

assay. (i) Representative CD4-gated or CD8-gated histograms of T cell proliferation assay in vitro based on the dilution of CFSE dye when T cells were stimulated by CD3/CD28 beads and/or cocultured with MDSCs at different ratio. (ii) Percentage suppression of MDSCs derived from S-PC tumor tissues on T cell proliferation. **(D)** Real-time PCR analysis for the expression of PD-1, PD-L1, CTLA-4, and CD86 mRNA expression in PPC, S-PC, and CRPC tissues collected from Myc-CaP allograft mouse models. Error bars represent mean ± SD; *n* = 3/group and analyzed by Student's *t* test. **, P < 0.01. **(E)** Growth curves of control and OBP2A-KD Myc-CaP allograft tumors in castrated FVB mice treated with anti–PD-1 monoclonal antibody. Error bars represent mean ± SD; *n* = 5/group and analyzed by Student's *t* test. **, P < 0.01. **(F)** Growth curves of control and OBP2A-KD Myc-CaP allograft tumors in castrated FVB mice treated with anti–CTLA-4 monoclonal antibody. Error bars represent mean ± SD; *n* = 5/group and analyzed by Student's *t* test. **, P < 0.01. Each panel in A–F is representative of at least two independent experiments. See also Fig. S4.

significantly improved the efficacy of anti–PD-1 and CTLA-4 antibody for the suppression of CRPC development in Myc-CaP allograft mouse models (Fig. 4, E and F; and Fig. S4, L and M).

The α-pinene interrupts the interaction of OBP2A with CXCL15/IL8 and inhibits PCa cell proliferation and migration

The α-pinene is a naturally occurring OBP2A-binding ligand found in the oils of coniferous trees, which is an alkene and contains a reactive four-membered ring structure (Begum et al., 2013; Briand et al., 2002; El Beyrouthy et al., 2015; Thang et al., 2014; Whitson and Whitson, 2014). It has been reported that α-pinene has antioxidant, antimicrobial, and anticancer activities (Aydin et al., 2013). To investigate the anticancer activity of α-pinene in PCa, OBP2A-KD, and control Myc-CaP cells cultured in charcoal-treated medium were treated with vehicle, CXCL15 (100 ng/ml), and/or α-pinene (1 µg/ml) for 72 h, and the cell proliferation rate was examined by MTT assay. We found that treatment with CXCL15 promoted the proliferation of Myc-CaP cells, while the addition of α-pinene completely blocked CXCL15-induced cell proliferation although treatment with α-pinene alone had minor effect on cell viability of Myc-CaP cells (Fig. 5 A). Furthermore, neither CXCL15 nor α-pinene had effects on OBP2A-KD Myc-CaP cells (Fig. 5 A). Similarly, treatment with IL8 promotes the proliferation of LNCaP cells, while the addition of α-pinene significantly blocked IL8-induced cell proliferation, and both IL8 and α-pinene had no effect on OBP2A-KD LNCaP cells (Fig. 5 B). In addition, transwell migration assay showed that treatment with α-pinene significantly reduced CXCL15-induced migration of Myc-CaP cells (Fig. 5 C and Fig. S5 A). These results indicate that α-pinene inhibits PCa cell proliferation and migration by interrupting the interaction between OBP2A and CXCL15/IL8.

Treatment with α-pinene inhibits MDSCs infiltration and CRPC development

As OBP2A knockdown reduced the infiltration of MDSCs in S-PC tumors (Fig. 4, A and B; and Fig. S4, A, B, F, and I–K), we asked whether treatment with α-pinene has the similar effect. As expected, transwell migration assay showed that treatment with α-pinene significantly decreased OBP2A-induced migration of monocytes (Fig. 5 D and Fig. S5 B). Similarly, coculture with LNCaP cells attracted the migration of U937 cells, treatment with α-pinene significantly impaired this effect (Fig. S5, C and D).

Importantly, treatment with α-pinene (40 mg/kg, i.v., every 3 d) significantly suppressed CRPC development in Myc-CaP allograft mouse models (Fig. 5 E and Fig. S5 E). Furthermore, the expression of CD11b, CXCR2, and Gr1 was significantly decreased in S-PC tissues collected from mice treated with α-pinene (Fig. 5 F). These results suggest that treatment with α-pinene inhibits the infiltration of MDSCs and suppresses CRPC development. It is worth noting that there were no apparent signs of toxicity in mice treated with α-pinene, as evidenced by body weight and other life symptom monitoring (Fig. S5 F).

The α-pinene–conjugated DOX (DOX-PIN) accumulates in S-PC tumors and shows stronger anticancer activity than unconjugated controls in mouse models

As OBP2A is highly accumulated in S-PC tumors, OBP2A ligand may function as a vehicle for drug delivery. To test this possibility, we linked α-pinene to DOX to produce DOX-PIN (Fig. 6 A and Fig. M1 in Data S1). FVB male mice with around 500 mm^3 Myc-CaP allograft tumors were castrated; 7 d later, mice were administrated i.v. with DOX or DOX-PIN (8 mg/kg), or vehicle. 2 h later, mice were sacrificed, and tumor tissue lysis were examined by ultra-high performance liquid chromatography–tandem mass spectrometry (UHPLC-MS/MS) for the content of DOX or DOX-PIN. We found that DOX-PIN in S-PC tissues was high, while DOX in S-PC tissues was undetectable (Fig. 6 B). As DOX has autofluorescence (Azarmi et al., 2006; Daga et al., 2016), tumor frozen sections were examined by fluorescent microscope for the red autofluorescence of DOX. We found that tumors collected from mice treated with DOX-PIN had much stronger red autofluorescence than DOX (Fig. 6 C).

To test the efficacy of DOX-PIN in mouse models, FVB male mice with 500 mm^3 Myc-CaP allograft tumors were castrated and treated with DOX or DOX-PIN (2 mg/kg, i.v., every 3 d). We found that treatment with unconjugated DOX had no clear effect on CRPC growth, while treatment with DOX-PIN significantly inhibited Myc-CaP CRPC development (Fig. 6 D and Fig. S5 G). Altogether, these results suggest that the engineered DOX with a conjugated α-pinene is specifically delivered and accumulated in S-PC tumors, resulting in a much stronger anticancer efficacy than non-conjugated DOX.

The α-pinene–conjugated DTX (DTX-PIN) has stronger anticancer efficacy than non-conjugated DTX

Currently, DTX, which functions as a microtubule inhibitor, is one of the major chemotherapies for CRPC and mCRPC, but it only modestly improves the survival time of PCa patients (Dayyani et al., 2011; Nader et al., 2018). We linked α-pinene to DTX to produce DTX-PIN (Fig. 6 E and Fig. M2 in Data S1). DTX and DTX-PIN showed similar toxicity in cancer cells in vitro. To test the efficacy of DTX-PIN in mouse models, FVB male mice with 500 mm^3 Myc-CaP allograft tumors were castrated and treated with DTX or DTX-PIN (10 mg/kg, i.v., every 3 d). We found that DTX-PIN had stronger inhibitory effect than DTX on CRPC growth and development (Fig. 6 F and Fig. S5, H and I). These results suggest that engineered DTX with a conjugated

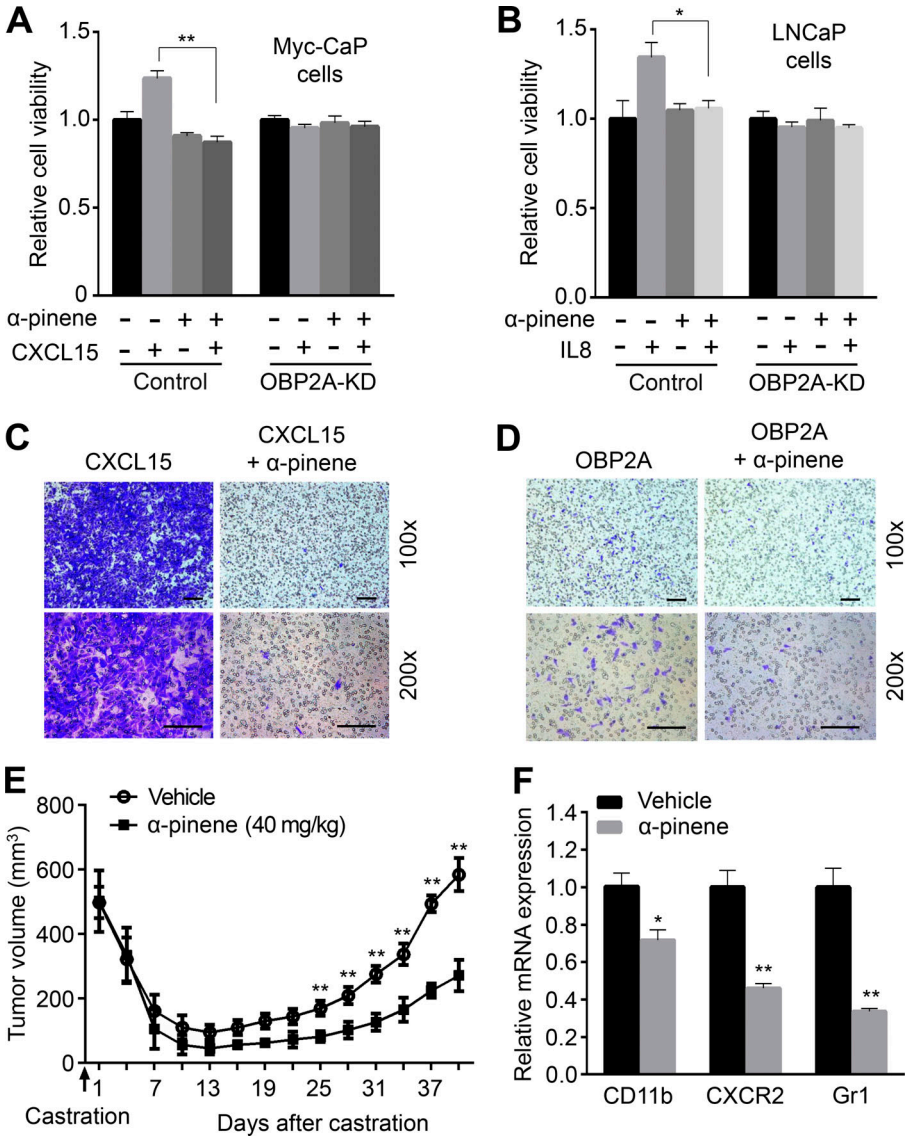

Figure 5. **α-pinene suppresses MDSCs infiltration and CRPC development through interrupting the interaction between OBP2A and CXCL15. (A)** MTT assay for the proliferation rate of Myc-CaP cells cultured in charcoal-treated medium and treated with vehicle, CXCL15 (100 ng/ml), and/or α-pinene (1 μg/ml) for 72 h. Error bars represent mean ± SD; *n* = 3/group and analyzed by Student's *t* test. **, P < 0.01. **(B)** MTT assay for the proliferation rate of control and OBP2A-KD LNCaP cells cultured in charcoal-treated medium and treated with vehicle, IL8 (100 ng/ml), and/or α-pinene (1 μg/ml) for 72 h. Error bars represent mean ± SD; *n* = 3/group and analyzed by Student's *t* test. *, P < 0.05. **(C)** Representative images of transwell migration assay for Myc-CaP cells treated with α-pinene (1 μg/ml) or vehicle in 1% charcoal-treated medium in the upper chamber, and 100 ng/ml CXCL15 or vehicle was added in the lower chamber. The scale bars represent 100 μm. **(D)** Representative images of transwell migration assay for monocyte RAW264.7 cells cultured in 1% charcoal-treated medium in the upper chamber, and 100 ng/ml OBP2A plus α-pinene (1 μg/ml) or vehicle was added in lower chamber. The scale bars represent 100 μm. **(E)** Growth curves of Myc-CaP allograft tumors in FVB mice castrated and started the treatment with vehicle or α-pinene (PIN, 40 mg/kg, every 3 d, i.v.) when tumor size reached 500 mm^3. Error bars represent mean ± SD; *n* = 5/group and analyzed by Student's *t* test. **, P < 0.01. **(F)** Real-time PCR analysis for the mRNA expression of CD11b, CXCR2, and Gr1 in S-PC tissues collected from Myc-CaP allograft mice treated with vehicle or α-pinene. Error bars represent mean ± SD; *n* = 3/group and analyzed by Student's *t* test. *, P < 0.05; **, P < 0.01. Each panel in A–F is representative of at least two independent experiments. See also Fig. S5.

α-pinene is specifically delivered to S-PC tumors, resulting in a much stronger anticancer efficacy than non-conjugated DTX.

Altogether, we have demonstrated that OBP2A secreted from PCa cells of tumors in remission during ADT can catch the survival factors, such as CXCL15/IL8, in TME to promote PCa androgen-independent growth and to attract the infiltration of MDSCs into tumors that results in a highly immunosuppressive TME, which together drive the emergence of PCa castration resistance (Fig. 7). To inhibit the emergence or delay the onset of PCa castration resistance, the naturally occurring OBP2A-binding ligand α-pinene can be either employed as a therapeutic agent that interrupts the interaction of OBP2A with survival factors, such as CXCL15/IL8, or as a delivery vehicle to transport conjugated therapeutic agents, such as DTX-PIN and DOX-PIN, specifically into S-PC tumors.

Discussion

ADT was first used about 80 yr ago and still remains the principal systemic treatment for patients with advanced PCa, as the majority of patients initially respond to ADT with a mean remission time of 2–3 yr. However, almost all cancers will eventually develop castration resistance (Crawford et al., 2019; Karantanos et al., 2013). ADT induces distinctive histologic changes in PCa cells of tumors in remission, including cytoplasmic clearing, nuclear and nucleolar shrinkage, and chromatin condensation (Bostwick et al., 2004). PCa cells of tumors in remission are more vulnerable than CRPC cells and the molecular life line in these cells may be ideal "preemptive" targets for the treatment of PCa castration resistance, however, tumors in remission are under-investigated and the molecular changes in these tumors are largely unknown. In the present study, we show that the OBP2A that is produced and released from PCa cells of tumors in remission during ADT drives the emergence of PCa castration resistance. Targeting OBP2A significantly delays the onset or emergence of PCa castration resistance.

OBP2A was firstly identified as an odorant carrier protein and plays a critical role in olfaction. The hydrophobic cavity within the beta-barrel of OBP2A facilitates OBP2A to catch small molecular odorants and to deliver them to olfactory receptors

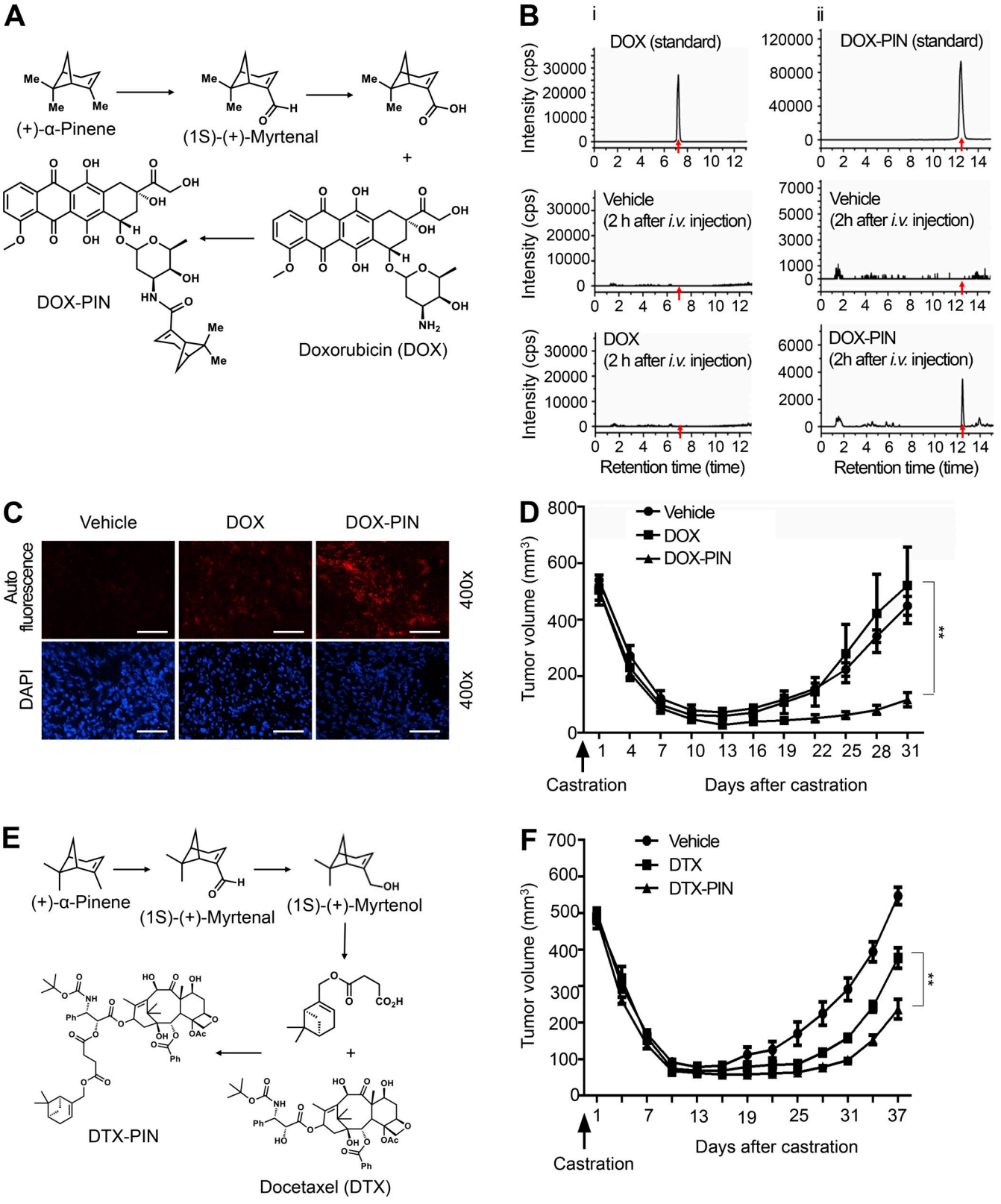

Figure 6. **DOX-PIN or DTX is specifically delivered to tumors, resulting in much strong potency than unconjugated controls. (A)** The diagram for the synthesis of DOX-PIN. **(B and C)** Myc-CaP allograft tumor-burden mice were castrated; 7 d later, mice were treated with DOX (8 mg/kg), DOX-PIN (8 mg/kg), or vehicle for 2 h, mice were sacrificed and tumor tissue lysis was examined by UHPLC-MS/MS analysis for the content of DOX (i, left) or DOX-PIN (ii, right; B), and the tumor frozen sections were examined by fluorescent microscope for autofluorescence (red) of DOX (C). The scale bars represent 50 µm. **(D)** Growth curves of Myc-CaP allograft tumors in FVB mice castrated and started the treatment with DOX or DOX-PIN (2 mg/kg, i.v., every 3 d) when tumor size reached 500 mm^3. Error bars represent mean ± SD; n = 5/group and analyzed by Student's t test. **, $P < 0.01$. **(E)** The diagram for the synthesis of DTX-PIN. **(F)** Growth

curves of Myc-CaP allograft tumors in FVB mice castrated and started the treatment with DTX or DTX-PIN (10 mg/kg, i.v., every 3 d) when tumor size reached 500 mm^3. Error bars represent mean ± SD; *n* = 5/group and analyzed by Student's *t* test. **, P < 0.01. Each panel in B–D and F is representative of at least two independent experiments. See also Fig. S5.

(Briand et al., 2002; Lacazette et al., 2000; Pelosi, 2001). The role of OBP2A in cancer is unclear. It has been reported that the expression of OBP2A is one of the five genes (ANGPTL7, OBP2A, SLC27A5, RP11-702B10.1, RP11-523H24.3) that can be used as a clinical multi-dimensional signature for predicting the prognosis of esophageal carcinoma (Guo et al., 2016). The fusion of OBP2A gene with its homologous gene OBP2B (OBP2A–OBP2B fusion), which is comprised of only three mispaired reads, is reported in PCa at the RNA level, however, the significance of this fusion in PCa is unknown as this fusion does not encode a fusion protein (Teles Alves et al., 2015). Our study demonstrates that OBP2A released by PCa cells of tumors in remission during ADT can catch the survival factors, such as CXCL15/IL8 (Araki et al., 2007; Neveu et al., 2014; Seaton et al., 2008; Zhao et al., 2005), to promote PCa cell androgen-independent growth and the infiltration of MDSCs into TME, leading to the emergence of PCa castration resistance.

OBP2A itself alone does not promote PCa cell proliferation, it is able to catch growth factors, such as CXCL15/IL8, in TME to promote the proliferation and mobility of PCa cells. This capability puts the role of OBP2A as unique and important in S-PC tumors, as S-PC cells themselves are "unprepared" to produce many survival factors and they do need OBP2A to catch these factors released from stromal cells in TME for survival under androgen-depletion conditions. Once they become castration-resistant, PCa cells themselves can produce their own survival factors and they can survive without the assistance of OBP2A. Indeed, our study shows that the expression of OBP2A is significantly decreased in CRPC cells as compared with S-PC cells.

MDSCs play important roles in the maintenance of the immunosuppressive TME through affecting the interactions between cancer cells and immune effectors, and are associated with tumor progression, metastasis, and poor clinical prognosis (Gabrilovich, 2017; Gabrilovich et al., 2012). MDSCs can not only produce various cytokines/chemokines that directly promote cancer cell proliferation and growth, but also release high levels of immune inhibitors, such as Arginase-1 that depletes L-arginine in TME, to suppress the anti-tumor immune function of dendritic cells and T cells (Zhong et al., 2020). In present study, we demonstrate that OBP2A knockdown decreases the infiltration of MDSCs into S-PC tumors, and significantly enhances the efficacy of PD-1 and CTLA-4 antibodies for the suppression of CRPC development, suggesting that combined ADT with anti–PD-1 or anti–CTLA-4 antibody treatment for human advanced PCa could be improved upon by OBP2A inhibition.

In physiological conditions, CXCL15/IL8 can be produced and secreted by many cell types, such as monocytes, endothelial cells, and various epithelial cells. In tumors, various stromal cells in TME, such as tumor-associated macrophages, tumor-associated adipocytes, tumor-associated pericytes, and MDSCs, secrete CXCL15/IL8 (Labani-Motlagh et al., 2020). Tumor cells, especially those becoming therapy-resistant, produce high level of CXCL15/IL8; elevated systemic and tumor-associated IL8 is associated with reduced clinical benefit of immune-checkpoint blockade (Schalper et al., 2020; Yuen et al., 2020). It has been reported that IL8 is related to PCa progression and androgen-independent PCa development. However, most of the reports focused on the role of IL8 that is expressed and/or secreted by cancer cells particularly by androgen-independent PCa cells or CRPC cells (Araki et al., 2007; Neveu et al., 2014; Seaton et al., 2008). Our study has demonstrated that CXCL15/IL8 expressed in S-PC tumors is mainly from stromal cells of TME and plays an important role in the transformation of PCa cells from androgen-dependent to androgen-independent state. OBP2A

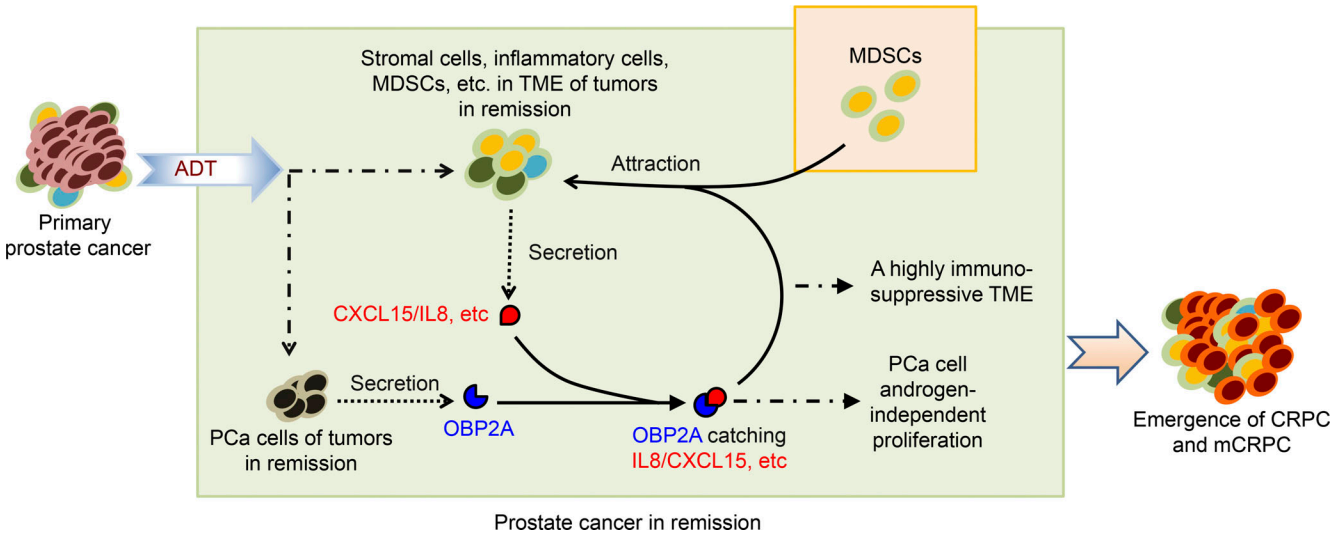

Figure 7. **Schematic representation for the role of OBP2A and its interaction with CXCL15/IL8 in TME in driving the emergence of CRPC and mCRPC.**

released from PCa cells can catch CXCL15/IL8 in TME to attract the infiltration of MDSCs into tumors that further increases the sources of CXCL15/IL8 in TME (as MDSCs secrete and release CXCL15/IL8), leading to PCa cell androgen-independent proliferation and growth and consequently the development of CRPC. During the evolution process, PCa cells gradually acquire the capability to produce survival factors, such as CXCL15/IL8, to adapt the new microenvironment for survival under ADT. Therefore, once they become castration-resistant, PCa cells themselves are able to produce CXCL15/IL8 for survival in the androgen-depletion environment (Lopez-Bujanda et al., 2021).

It has been reported that α-pinene has antioxidant, antimicrobial, and anticancer activities (Aydin et al., 2013). The anticancer activities of α-pinene may be related to its regulation of cell cycle, the antioxidation, the reduction of inflammation, and the induction of cell apoptosis (Matsuo et al., 2011; Yousuf Dar et al., 2012). Recently, high dose of α-pinene has been reported inhibits PCa growth in a xenograft mouse model (Zhao et al., 2018). In the present study, we demonstrate that treatment with α-pinene blocks the function of OBP2A and suppresses CRPC development in mouse models. Engineered DOX and DTX with a conjugated α-pinene are specifically delivered to and enriched in tumors during ADT, resulting in a much stronger anticancer efficacy than non-conjugated controls. Our study suggests that α-pinene itself would be a very good therapeutic agent for the suppression of the emergence of PCa castration resistance, it also can be used as a drug-delivery vehicle that guides and transports its conjugated toxic drug to be delivered specifically into S-PC tumors, which dramatically increases the potency while decreases the side effects of the drug.

Materials and methods

Cell culture

Myc-CaP, an androgen-sensitive PCa cell line derived from *c-Myc* transgenic mouse, LNCaP, and VCaP, a human prostate carcinoma cell lines, as well as U937 (ATCC) were cultured in RPMI-1640 medium supplemented with 1% antibiotic-antimycotic and 10% FBS; RAW 264.7 cells (ATCC) were cultured in DMEM/high glucose medium with 10% FBS and incubated at 37°C in a humidified atmosphere containing 5% CO_2; and SC cells (ATCC) were cultured in Iscove's modified Dulbecco's medium supplemented with 0.05 mM 2-mercaptoethanol, 0.1 mM hypoxanthine, and 0.016 mM thymidine with 10% FBS and incubated at 37°C in a humidified atmosphere containing 5% CO_2. Charcoal-stripped FBS was obtained from Sigma. Phenol red–free RPMI-1640 medium was purchased from Hyclone.

RNA-seq analysis

Total RNA was prepared with RNeasy Mini kit (QIAGEN) and quantified using the Qubit 2.0 Fluorometer (Invitrogen) and evaluated on the Agilent 2100 Bioanalyzer RNA nano chip (Agilent Technologies). All RNA samples were excellent quality with RNA Integrity Number >8.0. The DNase-treated Total RNA (300 ng input) was depleted of ribosomal RNA using probes provided by the NEBNext rRNA depletion module (#E6310L; NEB) according to manufacturer recommendations. The library preparation from the rRNA-depleted RNA was conducted according to NEBNextUltra II Directional RNA kit (#E7760; NEB) guidelines. The final libraries were validated on the bioanalyzer DNA chips, normalized to 2 nM, pooled equally and loaded onto the NextSeq 500 v2.5 flow cell at 1.8 pM final concentration and sequenced using 2 × 80 bp paired-end chemistry. On average, 20–25 million reads pass filter (base quality score >Q30 suggesting less than one error in 1,000 bp) are generated per sample. The RNA-seq data was deposited in the Gene Expression Omnibus under accession no. GSE208321.

RNA isolation and real-time PCR

RNA was prepared with RNase Mini kit (QIAGEN), and cDNA was synthesized using cDNA Synthesis Kits (Thermo Fisher Scientific). Quantitative real-time PCR (qRT-PCR) was performed using EvaGreen (Solis BioDyne) in the IQ5 BioRad thermocycler. The mRNA data were normalized for the amount of GAPDH using the $2^{-\Delta\Delta Ct}$ method. The data are presented as relative expression with the control set to 1. The data are presented as mean ± SD. Oligonucleotides used for qRT-PCR are shown in Table S1.

Western blot analysis

Cell or tissue lysates were separated by SDS-PAGE and transferred to polyvinylidene difluoride (PVDF) membranes. Immunostaining was done using antibodies specific for OBP2A (Lipocalin-13; R&D Systems), CXCL15 (WECHE, Santa Cruz Biotechnology), HA-tag (Cell Signaling Technology), and β-actin (Santa Cruz Biotechnology). Chemoluminescence detection was performed using the Pierce ECL Western Blotting Substrate (Thermo Fisher Scientific).

Immunohistochemistry (IHC)

The paraffin-embedded mouse prostate tumor tissue sections were stained with antibody against OBP2A (Lipocalin-13, R&D Systems). For the procedure of IHC, briefly, 5-μm-thick paraffin-embedded tissue sections were treated with an antigen retrieval solution (Sigma-Aldrich) and stained using VECTASTAIN ABC-HRP Kit (Vector Laboratories) according to the manufacturer's protocol. The tissue sections were incubated with the primary antibodies (1:1,000 dilution) in 10% blocking serum overnight at 4°C then incubated with biotinylated secondary antibody (1:500 dilution), followed by avidin-biotin peroxidase complex. Finally, tissue sections were stained with 3,3′-diaminobenzidine and counterstained with hematoxylin.

Transduction

Myc-CaP cells were transduced the lentiviral stocks using ViraDuctin Lentivirus Transduction Kit (Cell Biolabs) to stably express control shRNA (Sigma-Aldrich), and OBP2A shRNA Sigma-Aldrich), cultured in RPMI-1640 media supplemented with 10% FBS and puromycin (10 μg/ml).

Cell proliferation assay

Cell proliferation was measured using CellTiter 96 Non-Radioactive Cell Proliferation Assay kit (Promega) according to the

manufacturer's instructions. Briefly, after the cells cultured to different time points, the Dye Solution was added into the 96-well plates. The plates containing Dye Solution were incubated at 37°C cell culture incubator for 4 h. The Solubilization Solution/Stop Mix was added to the culture plates, and the plates were measured at 570 nm with reference wavelength of 630 nm using a 96-well plate reader.

Adenovirus transduction

Cells were transduced with GFP adenovirus or OBP2A-HA adenovirus from Applied Biological Materials Inc. at multiplicities of infection of 100 for 24 h in Gibco Opti-MEM Optimem media (Thermo Fisher Scientific), and then the media were replaced with RPMI-1640 media supplemented with 10% FBS. At 72 h after transduction, the transduction efficiency was confirmed by Western blot analysis, and these cells were used as temporary transduced cells.

Immunofluorescence (IF)

The paraffin-embedded mouse prostate tumor tissue sections were stained with antibody against OBP2A (Lipocalin-13; R&D Systems), CXCL15 (WECHE; Santa Cruz Biotechnology), CD3 (BD Biosciences), CD19 (BD Biosciences), F4/80 (Invitrogen), and Gr1 (Cell Signaling Technology). For the procedure of IF, briefly, 5-µm-thick paraffin-embedded tissue sections were treated with an antigen retrieval solution (Sigma-Aldrich). The tissue sections were incubated with the primary antibodies (1:1,000 dilution) in 10% blocking serum overnight at 4°C. Anti-Sheep IgG H&L (Alexa Fluor 594), Anti-Goat IgG H&L (Alexa Fluor 594), Anti-Rat IgG H&L (Fluorescein [FITC]) or Anti-Rabbit IgG H&L (Fluorescein [FITC]) secondary antibodies (Jackson ImmunoResearch Laboratories) were applied for 30 min at 37°C after washing thrice with PBS. DAPI was applied for 5 min at room temperature, and images were captured by a fluorescence microscope.

Immunoprecipitation

Shrunk prostate mouse tumor tissue lysates were incubated with the anti-OBP2A, anti-CXCL15, or control IgG antibodies followed by the addition of Protein A/G PLUS-Agarose beads (Santa Cruz Biotechnology) overnight at 4°C. Beads were washed three times with stringent buffer, and subsequently subjected to SDS-PAGE and transferred to PVDF membranes. Immunoblotting was performed with the indicated antibodies.

Transwell migration assay

Transwell inserts (#10464995 Greiner Bio-One ThinCert CellCoat; Thermo Fisher Scientific) coated with growth factor–reduced (GFR) Matrigel (BD Biosciences) were used for measurement of cell migration. Cells (1×10^3) were grown in phenol red–free RPMI-1640 media supplemented with 1% charcoal-stripped FBS in the upper side of the insert. The lower well was filled with phenol red–free RPMI-1640 media supplemented with 1% charcoal-stripped FBS and CXCL15 or IL8 (100 ng/ml; Huang et al., 2020). In addition, OBP2A overexpressed or knocked-down LNCaP cells were seeded in the lower chamber filled with phenol red–free RPMI-1640 medium supplemented with 1% charcoal-stripped FBS. Cells were incubated at 37°C in a humidified atmosphere containing 5% CO_2 for 48 h. Cells and Matrigel remnants located on the upper-insert membrane were removed, and invading cells from the lower side were fixed, stained, and analyzed according to the manufacturer's instructions.

In vitro suppression assays

MDSCs cells were isolated from S-PC tumor tissues of Myc-CaP allograft mouse models using EasySep Mouse MDSC Isolation Kit (StemCell Technologies) according to the manufacturer's instructions. Splenocytes containing $CD8^+$ or $CD4^+$ T cells derived from FVB mice were stained with 2.5 µM CFSE (AbMole) and seeded on a 24-well plate at 8×10^5 cells/well. MDSCs at different ratio were co-cultured with CFSE-labeled and CD3/CD28 beads activated T cells. 5 d later, the proliferation of T cell ($CD8^+CFSE^+$ or $CD4^+CFSE^+$) was measured by flow cytometry based on the dilution of CFSE.

Animal models

FVB mice were obtained from The Jackson Laboratory and maintained under specific pathogen–free conditions with phytoestrogen-free food and water ad libitum. Myc-CaP cells (1×10^6) in 50 µl sterile PBS were mixed with 50 µl GFR Matrigel (BD Biosciences), and the mixture was inoculated s.c. in the flanks of FVB mice. FVB male mice (6-wk-old) were used for castration model as described previously (Jeong et al., 2017). To obtain PPC cells, mice were euthanized when tumors reached a volume of 500 mm^3. Tumors were collected and tumor cells were isolated and purified using ACCUMAX (Innovative Cell Technologies) according to the manufacturer's instructions. To obtain S-PC cells, male mice with primary prostate tumor size of about 500 mm^3 were anesthetized and castrated as described previously (Jeong et al., 2017). After 7–10 d of castration, the mice were euthanized. Tumors were collected and tumor cells were isolated and purified using the same experimental procedure as for PPC cells. To obtain castration-resistant PCa cells (CRPC cells), male mice with primary prostate tumor size of about 500 mm^3 were anesthetized and castrated as described previously (Jeong et al., 2017). When tumors recurred and reached a volume of 500 mm^3 after castration, the mice were euthanized. Tumors were collected and tumor cells were isolated and purified using the same experimental procedure as for PPC cells. An orthotopic prostate tumor mouse model was used to determine intraprostate tumorigenicity. Subcutaneous tumors were harvested when they reached a volume of 500 mm^3 and were cut into pieces under aseptic conditions. After washing with PBS, the tumors were cut into cubes 1 mm^3 in size. One piece was then implanted on prostate tissue, between seminal vesicles, of each mouse. We monitored the living conditions of the mice daily. After 6 wk, the mice were euthanized and observed metastatic nodules in several tissues including liver, kidney, and lymph nodes. To evaluate the metastases, the lymph nodes and other distant organs, including liver, lung, stomach, intestine, kidney, and spleen, was examined under dissecting microscope. The distant organs were collected and fixed with 10% formalin. The fixed samples were then embedded in paraffin, and five non-

sequential serial sections were obtained per sample. The sections were stained with H&E and examined for the presence of metastases.

The castration-resistant PCa model was employed to assess the anti-cancer effect of newly synthesized compounds including DOX-PIN or DTX-PIN. Briefly, Myc-CaP cells (1×10^6) in 50 µl sterile PBS were mixed with 50 µl GFR Matrigel (BD Biosciences), and the mixture was inoculated s.c. in the flanks of FVB male mice (6-wk-old). The mice were castrated when tumors reached a volume of 500 mm^3. Before injection, DOX or DOX-PIN was diluted into 0.2 mg/ml with sterile H_2O. Then DOX or DOX-PIN were administered i.v. (2 mg/kg, 200 µl/mouse) by tail injection with syringe (EXELINT) every 3 d. Control mice were administered i.v. with same volume of vehicle. The treatment of PIN, DTX, or DTX-PIN was similar to that of DOX. Vehicle, anti–PD-1 mAb (10 mg/kg), or anti–CTLA-4 (10 mg/kg) was administered i.p. every 4 d, four times. Tumor volume was estimated by the formula volume = $(l \times w^2)/2$, where l stands for length and w stands for width.

For human PCa xenegraft mouse model, control and OBP2A knockdown (OBP2A-KD) LNCaP were inoculated into male *Rag1*$^{-/-}$ mice with subcutaneous slow-release 5-α-dihydrotestosterone pellet to generate androgen-dependent primary tumor. The mice were castrated and the testosterone pellet was removed when the tumor size was about 500 mm^3, then the tumor shrank to generate shrinking PCa and further regrew into castration-resistant tumors.

The PCa PDX models were established by implantation of the biopsy tissues of human PCa (AR-positive) into the sub-renal capsule of NOD-SCID male mice supplemented with testosterone. The tumor fragments from the first generation (F0) PDX tumors were transplanted s.c. into NOD-SCID male mice supplemented with testosterone to generate F1 PDX tumors. To examine whether OBP2A is increased in S-PC tumors in PDX models, a tumor tissue (2 mm^3) from F1 PDX tumors was grafted s.c. into right flank of 6-wk-old male NOD-SCID mice supplemented with testosterone (pellet, 10 mg/mouse). PDXs generated from three different human advanced PCa were used in the experiments.

The mouse experimental protocols were approved by the Scripps Florida Institutional Animal Care and Use Committee and followed the guidelines of the National Institute of Health.

UHPLC-MS/MS analysis

An Agilent 1260 HPLC system coupled with a 6230 time-of-flight liquid chromatography/mass spectrometry (LC/MS; Agilent Technologies) was used to analyze DOX or DOX-PIN. HPLC separation was performed with an Agilent Poroshell 120 EC-C18 column (50 × 4.6 mm I.D., 2.7 µm particle size; Agilent Technologies). Myc-CaP cells were inoculated s.c. in the flanks of 6-wk-old FVB mice, and the mice were castrated when tumors reached a volume of 500 mm^3. 7 d later, mice were i.v. treated with vehicle, DOX (8 mg/kg), or DOX-PIN (8 mg/kg) for 2 h, mice were sacrificed, and tumor tissues were collected. Tissue extracts were prepared by adding Tris-HCl buffer 50 mM pH 7.3, then were homogenized and sonicated in an ice bath for 10 min. To precipitate proteins, the mixture was added one volume of methanol, and then was centrifugated at 13,000 rpm at 4°C. The supernatant was used for UHPLC-MS/MS analysis. For DOX or DOX-PIN analysis, an optimized gradient elution for HPLC separation was used: 0–18 min, 5.0% B–100% B; 18–25 min, 100% B; where solvent A and solvent B were an aqueous solution of 0.1% HCOOH and 100% ACN, respectively. The flow rate was 0.4 ml/min. A negative ion mode and multiple reaction monitoring mode were adopted: m/z 542 for DOX and m/z 689 for DOX-PIN. The injection volume was 10 µl for each sample. The analysis of each sample was repeated at least three times.

Synthesis of compounds

Unless otherwise noted, all chemicals and reagents for chemical reactions were purchased at the highest commercial quality and used without further purification. Reactions were monitored by thin layer chromatography and LC/MS. Thin layer chromatography was performed with 0.25 mm E. Merck silica plates (60F-254) using short-wave UV light as the visualizing agent, $KMnO_4$, cerium ammonium molybdate, or phosphomolybdic acid and heat as developing agents. LC/MS was performed with Agilent 1260 Infinity System equipped with Poroshell 120 EC-C18 column (3.0 × 50 mm, 2.7 µm). Nuclear magnetic resonance (NMR) spectrums were recorded on a Bruker AVANCE AV400 (400 and 101 MHz) or Bruker AVANCE AV600 (600 and 151 MHz). Optical rotations were measured on Autopol IV polarimeter (Rudolph Research Analytical). The detail of the synthesis can be found in Data S1.

Quantification and statistical analysis

Differences between groups were examined for statistical significance using Student's *t* test. All P values are two-tailed, and $P < 0.05$ was considered statistically significant (*, $P < 0.05$; **, $P < 0.01$).

Online supplemental material

Fig. S1 shows the highly increased expression of OBP2A in S-PC during ADT. Fig. S2 shows the promotive role of OBP2A in the emergence of CRPC. Fig. S3 shows that OBP2A catches CXCL15/IL8 in TME to promote PCa cell androgen-independent growth and migration. Fig. S4 shows that OBP2A knockdown in PCa cells impairs the attraction to monocytes. Fig. S5 shows that the treatment with α-pinene impairs the attraction of cancer cells to monocytes. Table S1 contains the oligonucleotides used for qRT-PCR analysis. Data S1 shows synthesis details.

Declarations

Ethics approval

The mouse experimental protocols were approved by the Scripps Florida Institutional Animal Care and Use Committee and followed the guidelines of the National Institutes of Health.

Consent for publication

We have obtained consent to publish this paper from all the authors of this study.

Data availability

Source data are provided with this paper. All other data supporting the findings of the study are available from the corresponding authors upon request.

Acknowledgments

The authors thank Dr. Shohreh Iravani Dickinson at the Moffitt Cancer Center, Tampa, FL, USA, for kindly providing mouse tissue samples.

This work was supported by grants from National Institute of Health (R01CA140956, R01CA197944) and the United States Department of Defense (W81XWH-15-1-0235) to J.-L. Luo, and a postdoctoral trainee fellowship from the Frenchman's Creek Women For Cancer Research to J.H. Jeong.

Author contributions: Conceptualization, J.-H. Jeong, S. Zhong, and J.-L. Luo; Data curation, J.-L. Luo; Formal analysis, J.-H. Jeong and J.-L. Luo; Funding acquisition, J.-H. Jeong and J.-L. Luo; Investigation, J.-H. Jeong, S. Zhong, F. Li, C. Huang, X. Chen, Q. Liu, S. Peng, H. Park, Y.M. Lee, J. Dhillon, and J.-L. Luo; Methodology, J.-H. Jeong, S. Zhong, F. Li, C. Huang, X. Chen, Q. Liu, H. Park, S. Peng, and J.-L. Luo; Project administration, J.-L. Luo; Resources, J. Dhillon and J.-L. Luo; Supervision, J.-L. Luo; Validation, J.-H. Jeong and J.-L. Luo; Visualization, J.-H. Jeong and J.-L. Luo; Writing—original draft, J.-H. Jeong, S. Zhong, F. Li, and J.-L. Luo; Writing—review & editing, J.-H. Jeong, S. Zhong, X. Chen, and J.-L. Luo. All authors have read and approved the manuscript.

Disclosures: The authors declare no competing interests exist.

Submitted: 20 July 2021
Revised: 22 June 2022
Accepted: 17 November 2022

References

Alibhai, S.M., S. Gogov, and Z. Allibhai. 2006. Long-term side effects of androgen deprivation therapy in men with non-metastatic prostate cancer: A systematic literature review. *Crit. Rev. Oncol. Hematol.* 60: 201–215. https://doi.org/10.1016/j.critrevonc.2006.06.006

Amaral, T.M., D. Macedo, I. Fernandes, and L. Costa. 2012. Castration-resistant prostate cancer: Mechanisms, targets, and treatment. *Prostate Cancer*. 2012:327253. https://doi.org/10.1155/2012/327253

Ammirante, M., J.L. Luo, S. Grivennikov, S. Nedospasov, and M. Karin. 2010. B-cell-derived lymphotoxin promotes castration-resistant prostate cancer. *Nature*. 464:302–305. https://doi.org/10.1038/nature08782

Araki, S., Y. Omori, D. Lyn, R.K. Singh, D.M. Meinbach, Y. Sandman, V.B. Lokeshwar, and B.L. Lokeshwar. 2007. Interleukin-8 is a molecular determinant of androgen independence and progression in prostate cancer. *Cancer Res.* 67:6854–6862. https://doi.org/10.1158/0008-5472.CAN-07-1162

Aydin, E., H. Turkez, and F. Geyikoglu. 2013. Antioxidative, anticancer and genotoxic properties of alpha-pinene on N2a neuroblastoma cells. *Biologia*. 68:1004–1009. https://doi.org/10.2478/s11756-013-0230-2

Azarmi, S., X. Tao, H. Chen, Z. Wang, W.H. Finlay, R. Löbenberg, and W.H. Roa. 2006. Formulation and cytotoxicity of doxorubicin nanoparticles carried by dry powder aerosol particles. *Int. J. Pharm.* 319:155–161. https://doi.org/10.1016/j.ijpharm.2006.03.052

Begum, A., S. Sandhya, S. Shaffath Ali, K.R. Vinod, S. Reddy, and D. Banji. 2013. An in-depth review on the medicinal flora Rosmarinus officinalis (Lamiaceae). *Acta Sci. Pol. Technol. Aliment.* 12:61–73

Boettcher, A.N., A. Usman, A. Morgans, D.J. VanderWeele, J. Sosman, and J.D. Wu. 2019. Past, current, and future of immunotherapies for prostate cancer. *Front. Oncol.* 9:884. https://doi.org/10.3389/fonc.2019.00884

Bostwick, D.G., J. Qian, F. Civantos, C.G. Roehrborn, and R. Montironi. 2004. Does finasteride alter the pathology of the prostate and cancer grading? *Clin. Prostate Cancer*. 2:228–235. https://doi.org/10.3816/CGC.2004.n.004

Briand, L., C. Eloit, C. Nespoulous, V. Bézirard, J.C. Huet, C. Henry, F. Blon, D. Trotier, and J.C. Pernollet. 2002. Evidence of an odorant-binding protein in the human olfactory mucus: Location, structural characterization, and odorant-binding properties. *Biochemistry*. 41:7241–7252. https://doi.org/10.1021/bi015916c

Bronte, V., S. Brandau, S.H. Chen, M.P. Colombo, A.B. Frey, T.F. Greten, S. Mandruzzato, P.J. Murray, A. Ochoa, S. Ostrand-Rosenberg, et al. 2016. Recommendations for myeloid-derived suppressor cell nomenclature and characterization standards. *Nat. Commun.* 7:12150. https://doi.org/10.1038/ncomms12150

Cassetta, L., E.S. Baekkevold, S. Brandau, A. Bujko, M.A. Cassatella, A. Dorhoi, C. Krieg, A. Lin, K. Loré, O. Marini, et al. 2019. Deciphering myeloid-derived suppressor cells: Isolation and markers in humans, mice and non-human primates. *Cancer Immunol. Immunother.* 68:687–697. https://doi.org/10.1007/s00262-019-02302-2

Cho, K.W., Y. Zhou, L. Sheng, and L. Rui. 2011. Lipocalin-13 regulates glucose metabolism by both insulin-dependent and insulin-independent mechanisms. *Mol. Cell Biol.* 31:450–457. https://doi.org/10.1128/MCB.00459-10

Crawford, E.D., A. Heidenreich, N. Lawrentschuk, B. Tombal, A.C.L. Pompeo, A. Mendoza-Valdes, K. Miller, F.M.J. Debruyne, and L. Klotz. 2019. Androgen-targeted therapy in men with prostate cancer: Evolving practice and future considerations. *Prostate Cancer Prostatic Dis.* 22: 24–38. https://doi.org/10.1038/s41391-018-0079-0

Daga, M., C. Ullio, M. Argenziano, C. Dianzani, R. Cavalli, F. Trotta, C. Ferretti, G.P. Zara, C.L. Gigliotti, E.S. Ciamporcero, et al. 2016. GSH-targeted nanosponges increase doxorubicin-induced toxicity "in vitro" and "in vivo" in cancer cells with high antioxidant defenses. *Free Radic. Biol. Med.* 97:24–37. https://doi.org/10.1016/j.freeradbiomed.2016.05.009

Dayyani, F., G.E. Gallick, C.J. Logothetis, and P.G. Corn. 2011. Novel therapies for metastatic castrate-resistant prostate cancer. *J. Natl. Cancer Inst.* 103: 1665–1675. https://doi.org/10.1093/jnci/djr362

El Beyrouthy, B.Z.M., C. Safi, and O. Merah. 2015. Chemical composition of the essential oil of Satureja myrtifolia (Boiss. & Hohen.) from Lebanon. *J Essent Oil Bear Pl.* 18:248–254. https://doi.org/10.1080/0972060X.2014.890075

Gabrilovich, D.I. 2017. Myeloid-derived suppressor cells. *Cancer Immunol. Res.* 5:3–8. https://doi.org/10.1158/2326-6066.CIR-16-0297

Gabrilovich, D.I., S. Ostrand-Rosenberg, and V. Bronte. 2012. Coordinated regulation of myeloid cells by tumours. *Nat. Rev. Immunol.* 12:253–268. https://doi.org/10.1038/nri3175

Guo, J.-C., C.-Q. Li, Q.-Y. Wang, J.-M. Zhao, J.-Y. Ding, E.-M. Li, and L.-Y. Xu. 2016. Protein-coding genes combined with long non-coding RNAs predict prognosis in esophageal squamous cell carcinoma patients as a novel clinical multi-dimensional signature. *Mol. Biosyst.* 12:3467–3477. https://doi.org/10.1039/C6MB00585C

Huang, C., S. Zhong, H. Park, J.H. Jeong, and J.L. Luo. 2020. A simple and efficient system for producing recombinant human CXCL8 in *Escherichia coli*. *J. Interferon Cytokine Res.* 40:460–465. https://doi.org/10.1089/jir.2020.0021

Jeong, J.H., S.J. Park, S.I. Dickinson, and J.L. Luo. 2017. A constitutive intrinsic inflammatory signaling circuit composed of miR-196b, Meis2, PPP3CC, and p65 drives prostate cancer castration resistance. *Mol. Cell.* 65: 154–167. https://doi.org/10.1016/j.molcel.2016.11.034

Karantanos, T., P.G. Corn, and T.C. Thompson. 2013. Prostate cancer progression after androgen deprivation therapy: Mechanisms of castrate resistance and novel therapeutic approaches. *Oncogene*. 32:5501–5511. https://doi.org/10.1038/onc.2013.206

Labani-Motlagh, A., M. Ashja-Mahdavi, and A. Loskog. 2020. The tumor microenvironment: A milieu hindering and obstructing antitumor immune responses. *Front. Immunol.* 11:940. https://doi.org/10.3389/fimmu.2020.00940

Lacazette, E., A.M. Gachon, and G. Pitiot. 2000. A novel human odorant-binding protein gene family resulting from genomic duplicons at 9q34: Differential expression in the oral and genital spheres. *Hum. Mol. Genet.* 9:289–301. https://doi.org/10.1093/hmg/9.2.289

Lechner, M.G., D.J. Liebertz, and A.L. Epstein. 2010. Characterization of cytokine-induced myeloid-derived suppressor cells from normal human peripheral blood mononuclear cells. *J. Immunol.* 185:2273–2284. https://doi.org/10.4049/jimmunol.1000901

Lechner, M.G., C. Megiel, S.M. Russell, B. Bingham, N. Arger, T. Woo, and A.L. Epstein. 2011. Functional characterization of human $Cd33^{+}$ and $Cd11b^{+}$ myeloid-derived suppressor cell subsets induced from peripheral blood mononuclear cells co-cultured with a diverse set of human tumor cell lines. *J. Transl. Med.* 9:90. https://doi.org/10.1186/1479-5876-9-90

Lopez-Bujanda, Z.A., M.C. Haffner, M.G. Chaimowitz, N. Chowdhury, N.J. Venturini, R.A. Patel, A. Obradovic, C.S. Hansen, J. Jacków, J.P.

Maynard, et al. 2021. Castration-mediated IL-8 promotes myeloid infiltration and prostate cancer progression. *Nat. Cancer*. 2:803–818. https://doi.org/10.1038/s43018-021-00227-3

Matsuo, A.L., C.R. Figueiredo, D.C. Arruda, F.V. Pereira, J.A. Scutti, M.H. Massaoka, L.R. Travassos, P. Sartorelli, and J.H. Lago. 2011. α-Pinene isolated from Schinus terebinthifolius Raddi (Anacardiaceae) induces apoptosis and confers antimetastatic protection in a melanoma model. *Biochem. Biophys. Res. Commun.* 411:449–454. https://doi.org/10.1016/j.bbrc.2011.06.176

Montironi, R., R. Mazzucchelli, M. Scarpelli, A. Lopez-Beltran, and G. Mikuz. 2006. Prostate carcinoma I: Prognostic factors in radical prostatectomy specimens and pelvic lymph nodes. *BJU Int.* 97:485–491. https://doi.org/10.1111/j.1464-410X.2005.05972.x

Nader, R., J. El Amm, and J.B. Aragon-Ching. 2018. Role of chemotherapy in prostate cancer. *Asian J. Androl.* 20:221–229. https://doi.org/10.4103/aja.aja_40_17

Neveu, B., X. Moreel, M.P. Deschênes-Rompré, A. Bergeron, H. LaRue, C. Ayari, Y. Fradet, and V. Fradet. 2014. IL-8 secretion in primary cultures of prostate cells is associated with prostate cancer aggressiveness. *Res. Rep. Urol.* 6:27–34. https://doi.org/10.2147/RRU.S58643

Pelosi, P. 2001. The role of perireceptor events in vertebrate olfaction. *Cell. Mol. Life Sci.* 58:503–509. https://doi.org/10.1007/PL00000875

Pernar, C.H., E.M. Ebot, K.M. Wilson, and L.A. Mucci. 2018. The epidemiology of prostate cancer. *Cold Spring Harb. Perspect. Med.* 8:a030361. https://doi.org/10.1101/cshperspect.a030361

Salehi, B., S. Upadhyay, I. Erdogan Orhan, A. Kumar Jugran, S. L D Jayaweera, D. A Dias, F. Sharopov, Y. Taheri, N. Martins, N. Baghalpour, et al. 2019. Therapeutic potential of α- and β-pinene: A miracle gift of nature. *Biomolecules*. 9:738. https://doi.org/10.3390/biom9110738

Schalper, K.A., M. Carleton, M. Zhou, T. Chen, Y. Feng, S.-P. Huang, A.M. Walsh, V. Baxi, D. Pandya, T. Baradet, et al. 2020. Elevated serum interleukin-8 is associated with enhanced intratumor neutrophils and reduced clinical benefit of immune-checkpoint inhibitors. *Nat. Med.* 26:688–692. https://doi.org/10.1038/s41591-020-0856-x

Seaton, A., P. Scullin, P.J. Maxwell, C. Wilson, J. Pettigrew, R. Gallagher, J.M. O'Sullivan, P.G. Johnston, and D.J. Waugh. 2008. Interleukin-8 signaling promotes androgen-independent proliferation of prostate cancer cells via induction of androgen receptor expression and activation. *Carcinogenesis*. 29:1148–1156. https://doi.org/10.1093/carcin/bgn109

Sheng, L., K.W. Cho, Y. Zhou, H. Shen, and L. Rui. 2011. Lipocalin 13 protein protects against hepatic steatosis by both inhibiting lipogenesis and stimulating fatty acid β-oxidation. *J. Biol. Chem.* 286:38128–38135. https://doi.org/10.1074/jbc.M111.256677

So, A., M. Gleave, A. Hurtado-Col, and C. Nelson. 2005. Mechanisms of the development of androgen independence in prostate cancer. *World J. Urol.* 23:1–9. https://doi.org/10.1007/s00345-004-0473-1

Tcatchoff, L., C. Nespoulous, J.C. Pernollet, and L. Briand. 2006. A single lysyl residue defines the binding specificity of a human odorant-binding protein for aldehydes. *FEBS Lett.* 580:2102–2108. https://doi.org/10.1016/j.febslet.2006.03.017

Teles Alves, I., T. Hartjes, E. McClellan, S. Hiltemann, R. Böttcher, N. Dits, M.R. Temanni, B. Janssen, W. van Workum, P. van der Spek, et al. 2015. Next-generation sequencing reveals novel rare fusion events with functional implication in prostate cancer. *Oncogene*. 34:568–577. https://doi.org/10.1038/onc.2013.591

Thang, T.D., D.N. Dai, N.X. Luong, and I.A. Ogunwande. 2014. Constituents of essential oils from the leaves, stem barks and resins of Canarium parvum Leen., and Canarium tramdenanum Dai et Yakovl. (Burseracea) grown in Vietnam. *Nat. Prod. Res.* 28:461–466. https://doi.org/10.1080/14786419.2013.873435

Watson, P.A., K. Ellwood-Yen, J.C. King, J. Wongvipat, M.M. Lebeau, and C.L. Sawyers. 2005. Context-dependent hormone-refractory progression revealed through characterization of a novel murine prostate cancer cell line. *Cancer Res.* 65:11565–11571. https://doi.org/10.1158/0008-5472.CAN-05-3441

Whitson, K.B., and S.R. Whitson. 2014. Human odorant binding protein 2a has two affinity states and is capable of binding some uremic toxins. *Biochem. Anal. Biochem.* 3:1–7

Yang, J., C. Yan, A.E. Vilgelm, S.C. Chen, G.D. Ayers, C.A. Johnson, and A. Richmond. 2020. Targeted deletion of CXCR2 in myeloid cells alters the tumor immune environment to improve antitumor immunity. *Cancer Immunol. Res.* 9:200–213. https://doi.org/10.1158/2326-6066.CIR-20-0312

Yousuf Dar, M., W.A. Shah, S. Mubashir, and M.A. Rather. 2012. Chromatographic analysis, anti-proliferative and radical scavenging activity of Pinus wallichina essential oil growing in high altitude areas of Kashmir, India. *Phytomedicine*. 19:1228–1233. https://doi.org/10.1016/j.phymed.2012.07.015

Yuen, K.C., L.F. Liu, V. Gupta, S. Madireddi, S. Keerthivasan, C. Li, D. Rishipathak, P. Williams, E.E. Kadel III, H. Koeppen, et al. 2020. High systemic and tumor-associated IL-8 correlates with reduced clinical benefit of PD-L1 blockade. *Nat. Med.* 26:693–698. https://doi.org/10.1038/s41591-020-0860-1

Zhao, J., H. Zhu, C.H. Wong, K.Y. Leung, and W.S. Wong. 2005. Increased lungkine and chitinase levels in allergic airway inflammation: A proteomics approach. *Proteomics*. 5:2799–2807. https://doi.org/10.1002/pmic.200401169

Zhao, Y., R. Chen, Y. Wang, and Y. Yang. 2018. α-Pinene inhibits human prostate cancer growth in a mouse xenograft model. *Chemotherapy*. 63:1–7. https://doi.org/10.1159/000479863

Zhong, S., J.H. Jeong, Z. Chen, Z. Chen, and J.L. Luo. 2020. Targeting tumor microenvironment by small-molecule inhibitors. *Transl. Oncol.* 13:57–69. https://doi.org/10.1016/j.tranon.2019.10.001

Zhou, Y., and L. Rui. 2013. Lipocalin 13 regulation of glucose and lipid metabolism in obesity. *Vitam. Horm.* 91:369–383. https://doi.org/10.1016/B978-0-12-407766-9.00015-8

Supplemental material

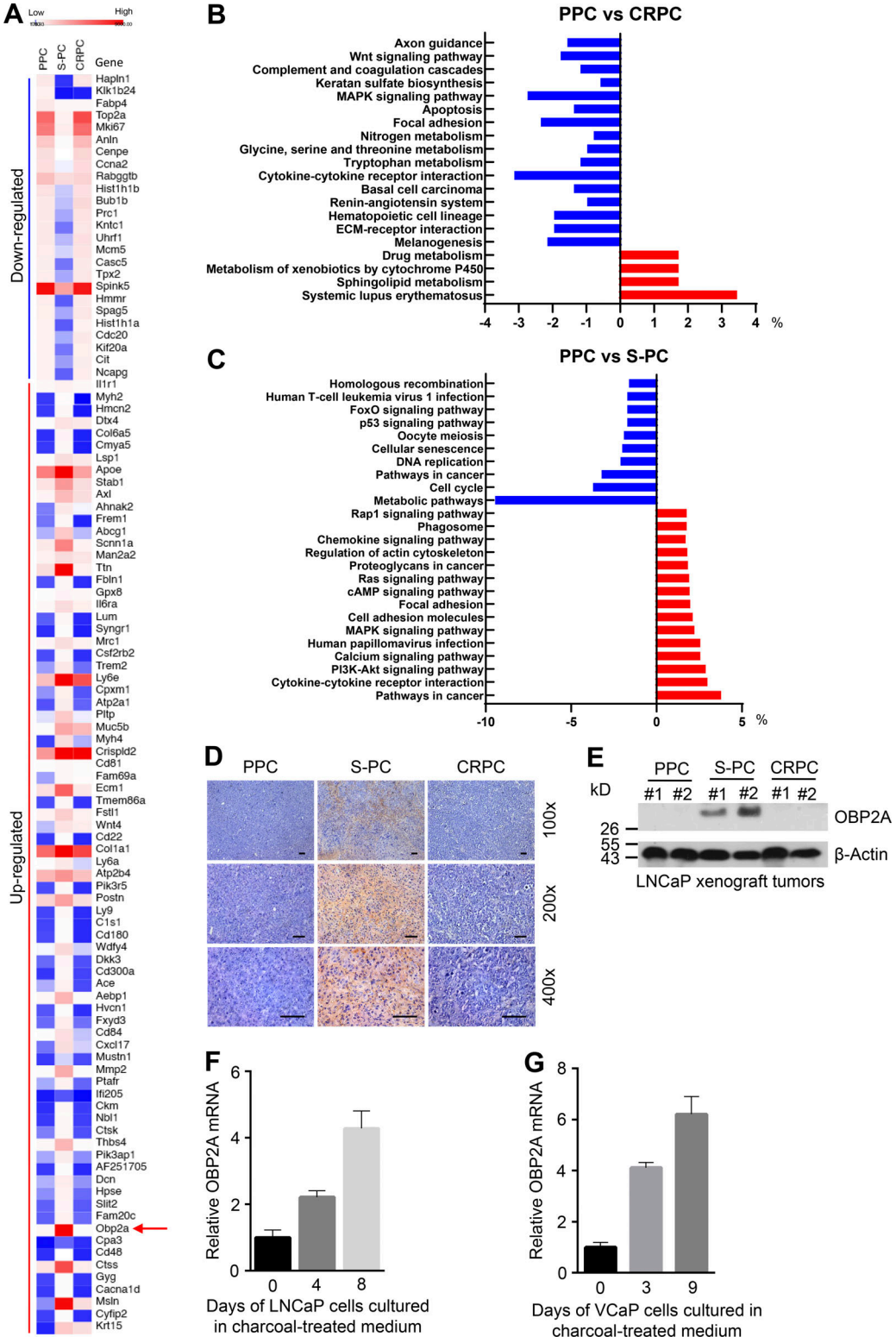

Figure S1. **The expression of OBP2A is highly increased in S-PC.** Related to Fig. 1. **(A)** Heatmap of differentially expressed genes in S-PC cells as compared with PPC and CRPC cells. Arrow indicates OBP2A gene. **(B and C)** KEGG pathway analysis of genes with differentially expressed in PPC vs. CRPC (B) and PPC vs. S-PC (C). The x axis displays the percentage of differentially expressed genes; the y axis indicates name of the pathway in the KEGG database. **(D)** IHC analysis for OBP2A protein expression in paraffin-embedded tissue sections of PPC, S-PC, and CRPC collected from Myc-CaP allograft mouse (FVB) models. The scale bars represent 50 µm. **(E)** Western blot analysis of OBP2A protein expression in PPC, S-PC, and CRPC tissues collected from human PCa LNCaP xenograft mouse (*Rag1*$^{-/-}$) models. **(F and G)** Real-time PCR analysis for OBP2A mRNA expression in LNCaP (F) and VCaP (G) cells cultured in charcoal-treated medium at different time points. Error bars represent mean ± SD; *n* = 3/group. Each panel in D–G is representative of at least two independent experiments. Source data are available for this figure: SourceData FS1.

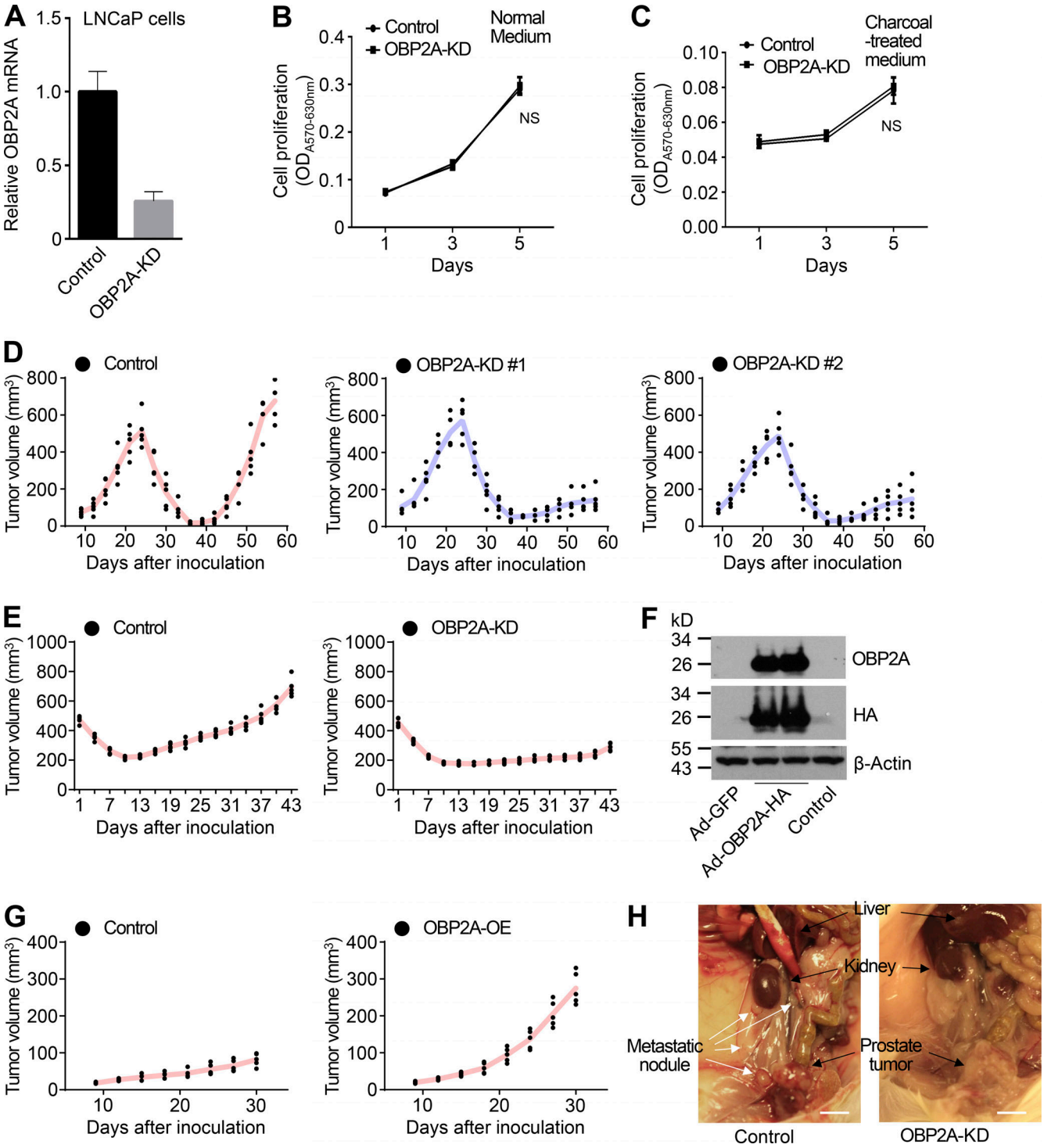

Figure S2. **OBP2A promotes the emergence of CRPC.** Related to Fig. 2. **(A)** Real-time PCR analysis for OBP2A mRNA expression in control and OBP2A-KD LNCaP cells cultured in charcoal-treated medium. Error bars represent mean ± SD; *n* = 3/group. **(B and C)** MTT assay for the proliferation rate of control or OBP2A-KD LNCaP cells cultured in normal (B) or charcoal-treated (C) medium. Error bars represent mean ± SD; *n* = 3/group and analyzed by Student's *t* test. **(D)** Related to Fig. 2 C. The graphs containing all individual tumors of allograft tumor development in FVB male mice inoculated with control (left), OBP2A-KD #1 (middle), and OBP2A-KD #2 (right) Myc-CaP cells. *n* = 5/group. **(E)** Related to Fig. 2 D. The graphs containing all individual tumors of xenograft tumor development in *Rag1*$^{-/-}$ male mice inoculated with control (left) and OBP2A-KD (right) LNCaP cells. *n* = 5/group. **(F)** Western blot analysis for the expression of exogenous HA-OBP2A in OBP2A-OE Myc-CaP cells. **(G)** Related to Fig. 2 G. The graphs containing all individual tumors of allograft tumor development in castrated FVB mice inoculated with control (left) and OBP2A-OE (right) Myc-CaP cells. *n* = 5/group. **(H)** A representative anatomical picture showing lymph node metastases in Myc-CaP orthotopic metastatic PCa model. The scale bars represent 0.5 cm. Each panel in A–H is representative of at least two independent experiments. Source data are available for this figure: SourceData FS2.

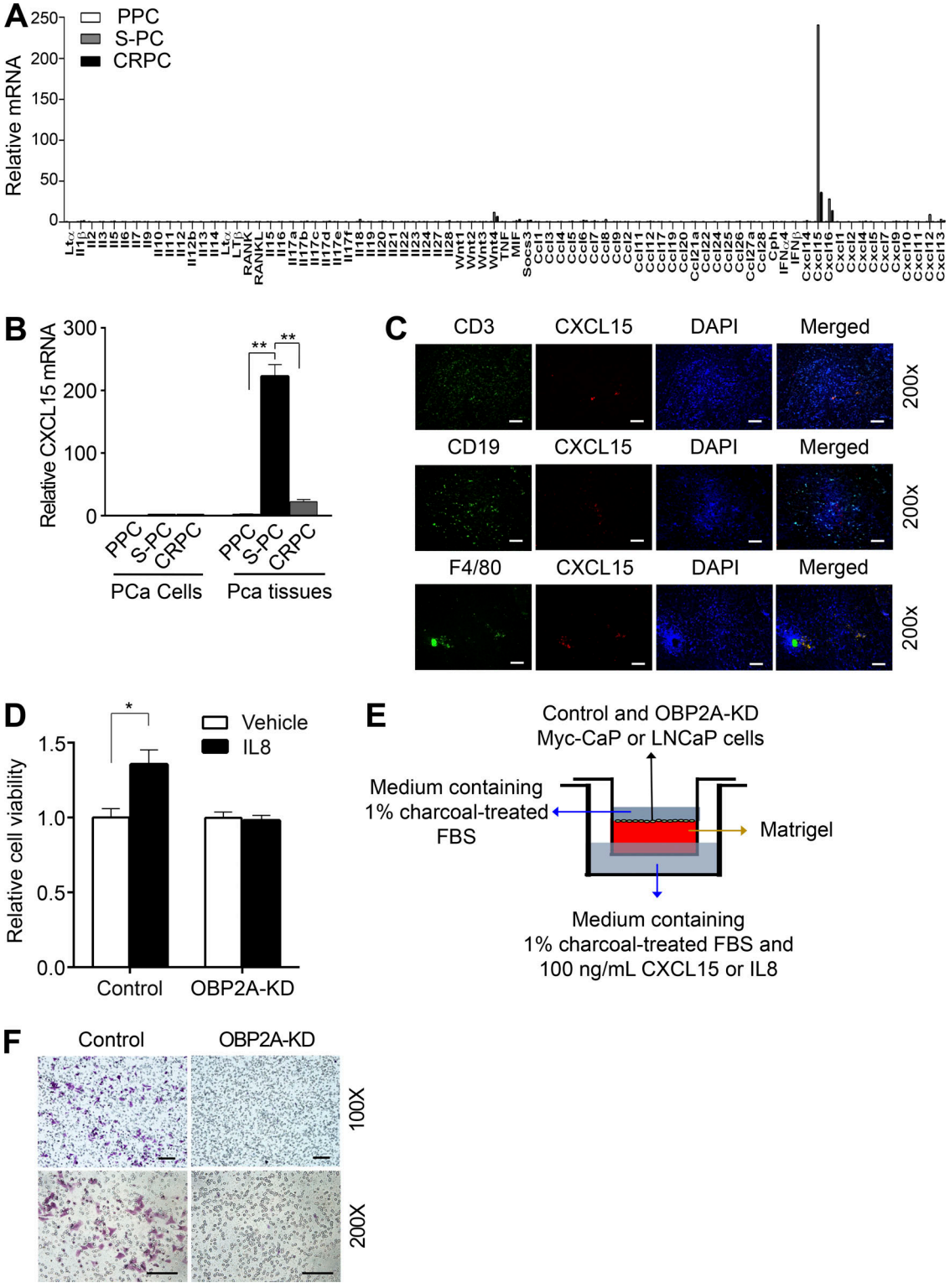

Figure S3. **OBP2A catches CXCL15/IL8 in TME to promote cancer cell proliferation and migration.** Related to Fig. 3. **(A)** Real-time PCR analysis for the mRNA expression of indicated genes in PPC, S-PC, and CRPC tissues. **(B)** The comparison of CXCL15 mRNA expression in purified PCa cells and PCa tissues collected from Myc-CaP allograft mouse models. Error bars represent mean ± SD; *n* = 3/group and analyzed by Student's *t* test. **, P < 0.01. **(C)** Representative images of IF staining of CXCL15, CD3, CD19, and F4/80 in paraffin-embedded tissue sections of S-PC collected from Myc-CaP allograft mouse models. The scale bars represent 50 µm. **(D)** MTT assay for the proliferation rate of control and OBP2A-KD LNCaP cells cultured in charcoal-treated medium and treated with IL8 (100 ng/ml) or vehicle for 72 h. Error bars represent mean ± SD; *n* = 3/group and analyzed by Student's *t* test. *, P < 0.05. **(E)** Schematic illustration of transwell migration analysis for control and OBP2A-KD Myc-CaP or LNCaP cells in response to CXCl15/IL8 (100 ng/ml) added in the lower chamber. **(F)** Representative images of transwell migration assay for control and OBP2A-KD LNCaP cells cultured in 1% charcoal-treated medium, and IL8 (100 ng/ml) or vehicle was added in the lower chamber. The scale bars represent 100 µm. Each panel in B–F is representative of at least two independent experiments.

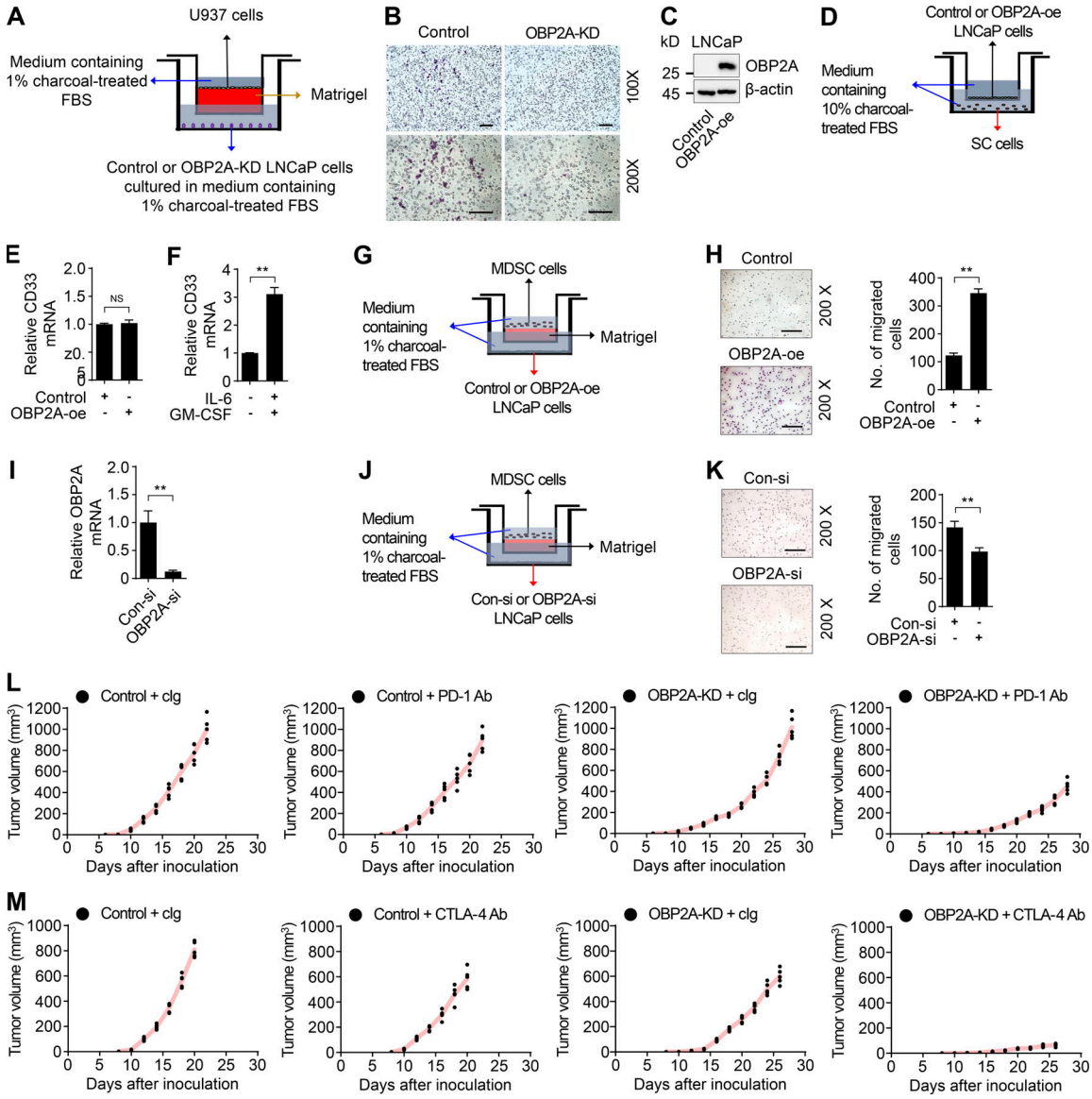

Figure S4. **OBP2A knockdown in cancer cells impairs the attraction to monocytes.** Related to Fig. 4. **(A)** Schematic illustration of transwell migration analysis for U937 cells in response to control and OBP2A-KD LNCaP cells cultured in the lower chamber containing 1% charcoal-treated FBS. **(B)** Representative images of transwell migration assay for U937 cells in response to control and OBP2A-KD LNCaP cells cultured in the lower chamber containing 1% charcoal-treated FBS. The scale bars represent 100 µm. **(C)** Western blot analysis for OBP2A expression in LNCaP cells transfected with control vector (control) or OBP2A expression (OBP2A-oe) plasmid for 48 h. **(D)** Schematic illustration of co-culture system for SC cells in response to control or OBP2A-oe LNCaP cells cultured in the upper chamber containing 10% charcoal-treated FBS. **(E)** qRT-PCR analysis for the expression of CD33 in SC cells from D. Error bars represent mean ± SD; *n* = 3/group and analyzed by Student's *t* test. **(F)** qRT-PCR analysis for the expression of CD33 in SC cells cultured with IL6 (10 ng/ml) and GM-CSF (10 ng/ml) for 7 d. Error bars represent mean ± SD; *n* = 3/group and analyzed by Student's *t* test. **, P < 0.01. **(G)** Schematic illustration of transwell migration analysis for MDSCs in response to control or OBP2A-oe LNCaP cells cultured in the lower chamber containing 1% charcoal-treated FBS. **(H)** Representative images (left) and migrated cells analysis (right) of transwell migration assay for MDSCs from G. The scale bars represent 100 µm. Error bars represent mean ± SD; *n* = 3/group and analyzed by Student's *t* test. **, P < 0.01. **(I)** qRT-PCR analysis for the expression of OBP2A in LNCaP cells transfected with scrambled (Con-si) or OBP2A siRNA (OBP2A-si) for 48 h. Error bars represent mean ± SD; *n* = 3/group and analyzed by Student's *t* test. **, P < 0.01. **(J)** Schematic illustration of transwell migration analysis for MDSCs in response to scrambled (Con-si) or OBP2A siRNA (OBP2A-si) LNCaP cells cultured in the lower chamber containing 1% charcoal-treated FBS. **(K)** Representative images (left) and migrated cells analysis (right) of transwell migration assay for MDSCs from J. The scale bars represent 100 µm. Error bars represent mean ± SD; *n* = 3/group and analyzed by Student's *t* test. **, P < 0.01. **(L)** Related to Fig. 4 E. The graphs containing all individual tumors of allograft tumor development. Control Myc-CaP allograft tumors in castrated FVB mice treated with clg (first panel, from the left), control Myc-CaP allograft tumors in castrated FVB mice treated with anti–PD-1 monoclonal antibody (second panel), OBP2A-KD Myc-caP allograft tumors in castrated FVB mice treated with clg (third panel), and OBP2A-KD Myc-caP allograft tumors in castrated FVB mice treated with anti–PD-1 monoclonal antibody (fourth panel). *n* = 5/group. **(M)** Related to Fig. 4 F. The graphs containing all individual tumors of allograft tumor development. Control Myc-CaP allograft tumors in castrated FVB mice treated with clg (first panel, from the left), control Myc-CaP allograft tumors in castrated FVB mice treated with anti–CTLA-4 monoclonal antibody (second panel), OBP2A-KD Myc-caP allograft tumors in castrated FVB mice treated with clg (third panel), and OBP2A-KD Myc-caP allograft tumors in castrated FVB mice treated with anti–CTLA-4 monoclonal antibody (fourth panel). *n* = 5/group. Each panel in A–M is representative of at least two independent experiments. Source data are available for this figure: SourceData FS4.

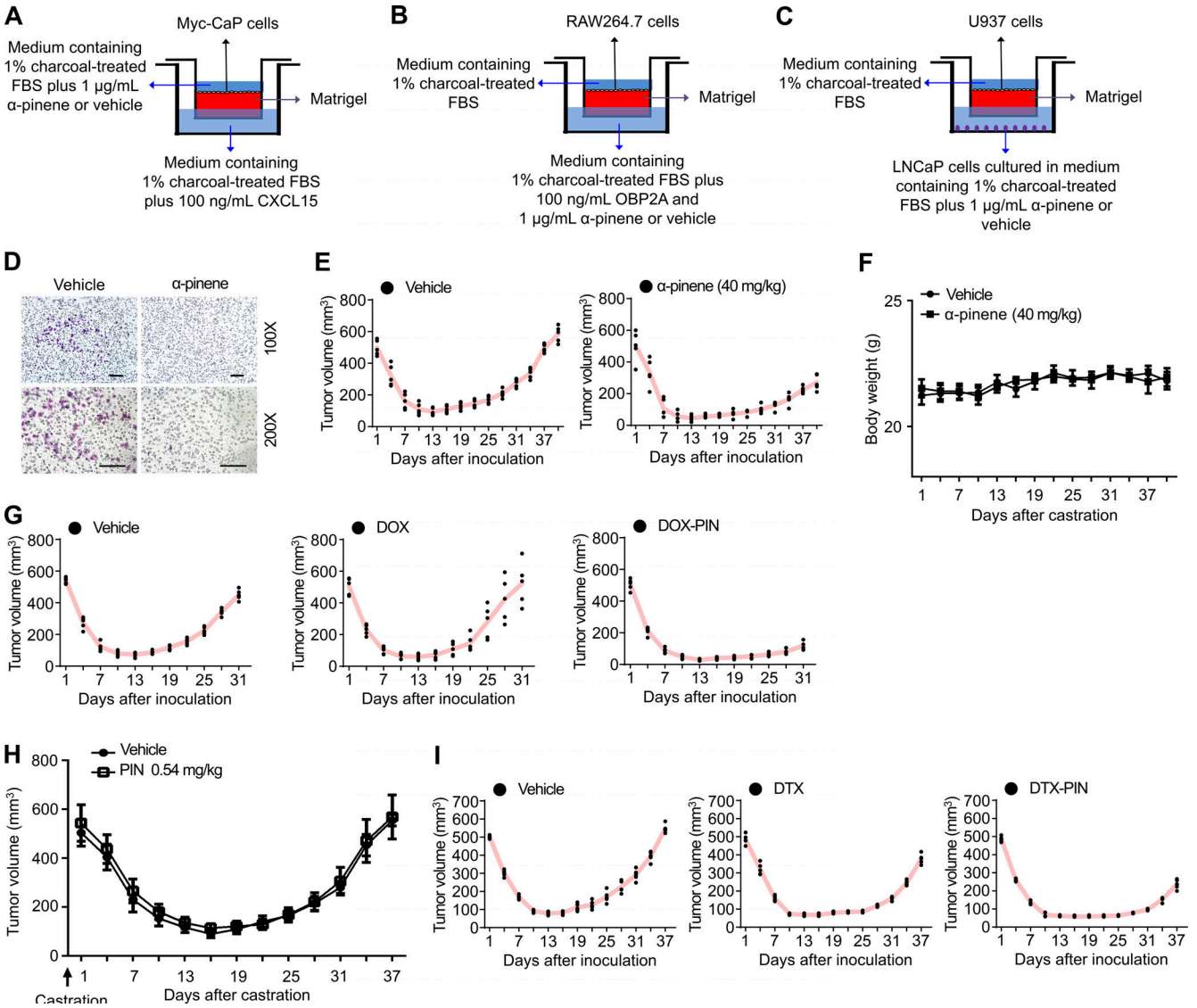

Figure S5. **Treatment with α-pinene impairs the attraction of cancer cells to monocytes.** Related to Figs. 5 and 6. **(A)** Schematic illustration of transwell migration analysis for Myc-CaP cells, treated with α-pinene (1 μg/ml) or vehicle in 1% charcoal-treated medium in the upper chamber, in response to 100 ng/ml CXCL15 or vehicle added in the lower chamber. **(B)** Schematic illustration of transwell migration analysis for monocyte RAW264.7 cells in response to OBP2A plus α-pinene or vehicle added in the lower chamber. **(C)** Schematic illustration of transwell migration analysis for U937 cells in response to LNCaP cells cultured in the lower chamber containing 1% charcoal-treated FBS plus 1 μg/ml α-pinene or vehicle. **(D)** Representative images of transwell migration assay for U937 cells in response to LNCaP cells cultured in the lower chamber containing 1% charcoal-treated FBS plus 1 μg/ml α-pinene or vehicle. The scale bars represent 100 μm. **(E)** Related to Fig. 5 E. The graphs containing all individual tumors of Myc-CaP allograft tumor development in castrated FVB mice treated with vehicle (left) or α-pinene (right). *n* = 5/group. **(F)** The body weight (BW) curve of mice treated with α-pinene or vehicle, related to Fig. 5 E. *n* = 5/group. **(G)** Related to Fig. 6 D. The graphs containing all individual tumors of Myc-CaP allograft tumor development in castrated FVB mice treated with vehicle (left), Dox (middle), or DOX-PIN (right). *n* = 5/group. **(H)** Myc-CaP cells were inoculated in the right flank of FVB male mice; when tumor size reached 500 mm^3, mice were castrated and treated with vehicle or α-pinene (PIN, 0.54 mg/kg), i.v., every 3 d. Tumor development in mice was monitored and measured every 3 d. *n* = 5/group. **(I)** Related to Fig. 6 F. The graphs containing all individual tumors of Myc-CaP allograft tumor development in castrated FVB mice treated with vehicle (left), DTX (middle), or DTX-PIN (right). *n* = 5/group. Each panel in A–I is representative of at least two independent experiments.

Provided online are Data S1 and Table S1. Data S1 shows the compound synthesis details. Table S1 lists oligonucleotides used for qRT-PCR analysis used in the study.